Table 4. Patterns of recurrence according to the radiation fields

Radiation fields	Total numbers of patients	Controlled (%)	Sites of recurrence		
			Local (%)	Regional lymph nodes (%)	Progression to MM or distant metastases (%)
Primary tumor	51	29	4*	1	21*
Primary tumor and regional lymph nodes	16	13	1	0	2
Total	67	42 (62)	5 (7.5)	1 (1.5)	23 (34)

Abbreviation: MM = multiple myeloma.
*4 patients experienced both local recurrence and progression to MM.

time from diagnosis to local recurrence was 65 months (median, 52 months). The overall 5- and 10-year local control (LC) rates were 95% and 87%, respectively (Fig. 1A). Only a single patient recurred locally, whereas 4 other patients had both local and distant diseases. Of 5 patients who developed local recurrences, 3 died of the disease. Regarding 2 other patients who experienced local recurrence, 1 was successfully treated and is alive without disease and the other developed multiple myeloma. Next, among 44 patients who treated radiotherapy and without surgery, influence of tumor size on local controllability was evaluated. Although 2 patients were excluded because their tumor size was not exactly determined, the tumor size was not a significant factor for the local control in the 42 patients ($p = 0.46$, Fig. 1B).

Disease progression and progression to MM

Disease progression was observed in 36% of patients (25 of 67). The 5- and 10-year DFS rates were 56% and 54%, respectively (Fig. 2). Among patients with disease progression, 8 patients (12%) were diagnosed with progression to MM. The median duration of progression to MM was 18 months (range, 6–71 months). Among other 17 patients, 1 experienced local recurrence alone, 4 patients did both local and distant recurrence, and 12 did distant recurrence alone. Next, patterns of failure sites and the radiation fields were investigated (Table 4). Only 1 patient who was treated to the primary tumor site without regional lymph nodes irradiation experienced regional lymph nodes recurrence, while none who were irradiated both primary and regional lymph nodes did. Salvage treatment was performed as follows: radiotherapy in 7 patients, chemotherapy in 9 patients, and surgery in 2 patients (including a patient treated with chemotherapy and surgery). The remaining 7 patients were followed only by careful observation.

Survival

The overall 5- and 10-year survival rates were 73% and 56%, respectively (Fig. 3). The cause-specific 5- and 10-year survival rates were 82% and 76%, respectively. At last follow-up, 18 patients had died. Among those patients, 10 (15%) had died of the disease, whereas 8 patients (12%) died of other diseases.

Prognostic factors for overall survival

Several factors were evaluated to determine whether they influenced overall survival. Radiotherapy combined with surgery was identified as the lone significant prognostic factor for overall survival (OS) ($p = 0.04$), whereas tumor size, age, gender, radiation dose, and chemotherapy were not predictive (Fig. 4, Table 5). To exclude the possibility

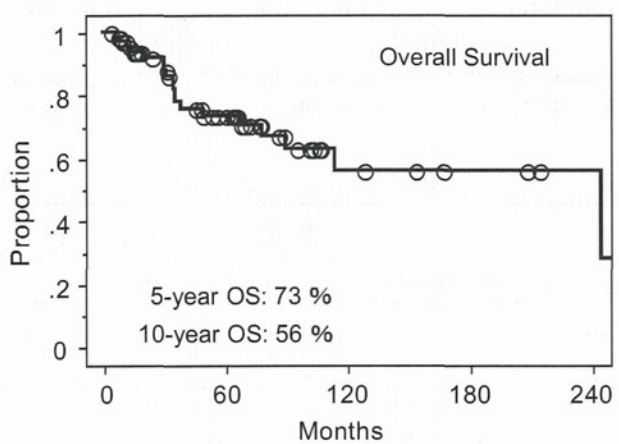

Fig. 3. Overall survival rate for extramedullary plasmacytoma of the head and neck (EMPHN) ($n = 67$).

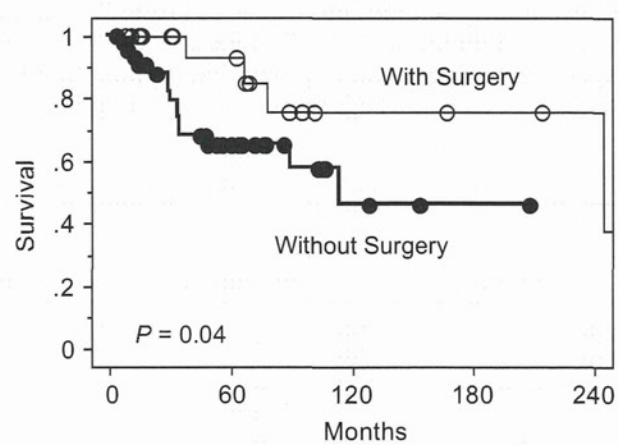

Fig. 4. Overall survival rates according to patients who received radiotherapy either with surgery ($n = 23$) or without surgery ($n = 44$).

Table 5. Prognostic factors for overall survival

Prognostic factors	*p* value
Tumor size	
≤5 cm (n = 45) vs. >5 cm (n = 13)	0.59
Age	
≤50 (n = 15) vs. >51 (n = 52)	0.3
Gender	
Male (n = 43) vs. female (n = 24)	0.95
Radiation dose	
≤40 Gy (n = 13) vs. >40.1 Gy (n = 54)	0.82
≤45 Gy (n = 17) vs. >45.1 Gy (n = 50)	0.73
≤50 Gy (n = 56) vs. >50.1 Gy (n = 11)	0.72
Surgery	
With surgery (n = 23) vs. without surgery (n = 44)	0.04
Chemotherapy	
With chemotherapy (n = 9) vs. without chemotherapy (n = 58)	0.75

of selection bias, an influence of age was evaluated. As shown in the Table 2, the cohorts of patients who were treated radiotherapy combined without surgery, and of patients with surgery, proportions of younger subgroup (≤50 years) and that of older subgroup did not differ significantly (p = 0.93). Of course, although larger numbers of cases and prospective studies will be needed, our results (Fig. 4) might not be influenced by a selection bias especially in regard with age.

Morbidities associated with radiotherapy

Acute morbidity was examined according to CTCAE version 3.0. Data regarding radiation dermatitis and radiation mucositis were obtained from 44 (66%) patients. Of these, 8 patients had Grade 2 radiation dermatitis, and 27 patients had Grade 1 radiation dermatitis (Table 6). A single patient experienced Grade 3 radiation mucositis, 13 patients experienced Grade 2, and 20 patients experienced Grade 1. No patient experienced morbidity after radiotherapy.

Table 6. Adverse effects after the radiotherapy according to CTCAE ver. 3.0

	Grade					
	0	1	2	3	4	5
Dermatitis	9	27	8	0	0	0
Mucositis	10	20	13	1	0	0

A case successfully treated with radiotherapy combined with surgery

A 70-year-old male suffered from a vast tumor located in the nasal cavity and extending to the paranasal cavity. At first, a radical surgery was planned, but the planned procedure seemed to be extremely invasive because the tumor had invaded into the base of the skull. Therefore, radiotherapy was employed as an initial treatment for this disease, and a total of 60 Gy (in 30 fractions over 6 weeks) was delivered using three-dimensional conformal radiotherapy (Fig. 5). At 3 months after the completion of radiotherapy, a residual tumor was observed at the concha nasalis media, and a less invasive tumorectomy was performed. The case was not expected to be cured by a single modality (either surgery or radiotherapy), but radiotherapy combined with surgery was successfully applied to the extensive EMPHN tumor (>5 cm in diameter) (Fig. 6).

DISCUSSION

Our study represents one of the largest in terms of scale (that is, a large number of patients with solitary EMP of the head or neck regions treated at multiple institutions with sufficient follow-up duration) (Table 7).

Solitary EMP is believed to be radiosensitive. However, because of the rarity of the disease, there have been few reports concerning the effective radiation dose. Several investigators have reported that local control rates of 80–100% are consistently found after moderate doses of radiotherapy (2–4, 25, 29–37). Tsang *et al.* (29) achieved local control in 13 of 14 (93%) of patients with a dose of 35 Gy. The only failure was in a patient with a large primary tumor (>5 cm). Similarly, Jyothirmayi *et al.* (30) achieved local control in 6 of 7 patients with doses of 35–45 Gy (median dose, 40 Gy in 20 fractions). The only failure was in a patient

Table 7. Comparison and reviews of literatures for plasmacytoma of the head and neck

						OS (%)		LCR (%)		DFS (%)	
Series (ref.)	Year	Institution	Numbers of patients	Follow-up (m)	Dose (median)	5-y	10-y	5-y	10-y	5-y	10-y
Liebross (4)	1999	Single	22	44	40–60 (50)	73	50	95	95	56	NA
Chao (37)	2005	Single	16	66	40–50.4 (45)	85	54	100	100	75	75
Tournier-Rangeard (32)	2006	Single	17	80	40–65 (52.6)	82	63	88	73	64	54
Bachar (41)	2008	Single	68	96	10–50 (35)	76	56	91	88	NA	NA
Creach (34)	2009	Single	18	82	34–56 (50.4)	80	54	NA	NA	74	53
Present study	2010	Multiple	67	63	30–60 (50)	73	56	95	87	56	54

Abbreviations: DFS = disease-free survival; LCR = local control rate; OS = overall survival.

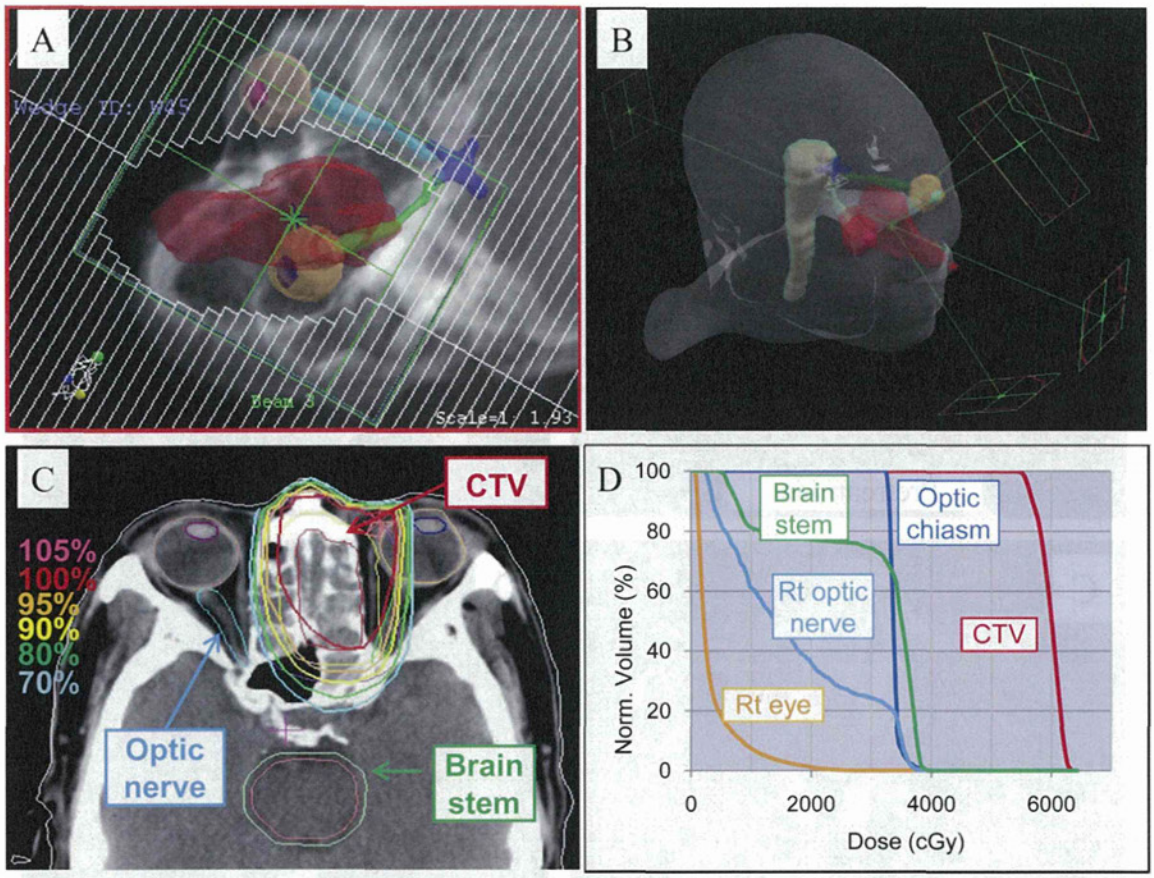

Fig. 5. A 70-year-old male patient suffered from a vast extramedullary plasmacytoma (EMP) located in the nasal and the paranasal cavities treated by three-dimensional conformal radiotherapy (3D-CRT). (A) A port of the 3D-CRT avoiding right optic nerve, right eye, and optic chiasm. (B) Directions and images of the five ports illustrated by using Xio software. (C) The isodose curves for the patient. (D) The dose–volume histogram (DVH) of the 3D-CRT plan.

with an extensive nasopharyngeal tumor. Holland *et al.* (25) also reported poorer local control in tumors >5 cm and similarly observed no evidence of a radiation dose–response effect over a dose range of 16–62 Gy (median dose, 46 Gy). Several series have reported 100% local control rates. Bolek *et al.* (31) reported 100% local control in 10 patients with doses ranging from 9 to 50 Gy (median dose, 45 Gy) and concluded by recommending a dose of 40 Gy in 20 fractions. Shih *et al.* (3) reported on 10 patients with SEP, seven of whom were treated with radiotherapy, using doses of 47–65 Gy. Tounier-Rangeard *et al.* (32) reported that a minimum dose of 45 Gy is recommended to the clinical target volume (CTV) of an EMPHN tumor. Mendenhall *et al.* (33) reported a study of 81 patients composed of a literature review and their own patients. These authors found a local control rate of 94% when the dose to the CTV was greater than 40 Gy and a rate of 69% when the dose to the CTV was less than 40 Gy. Creanch *et al.* (34) reported excellent local control in their series of 16 consecutive patients receiving a median dose of 50.4 Gy. The optimal radiation dose recommended by the UK Myeloma Forum in their 2004 guidelines is in the range of 40–50 Gy (35). In the guideline, tumors with SEP <5 cm have an excellent chance of local control with radiation doses of approximately 40 Gy in 20 fractions. There is a higher risk of local failure in tumors >5 cm, which require a higher dose (approximately 50 Gy in 25 fractions). From these previous investigations, it seems that the optimal radiation dose is in the range of 40–50 Gy, although tumor size might be a critical factor affecting local control. In our series from multiple institutions, with a similar median dose of 50 Gy administered (range, 30–60 Gy), the local control rate was similar and consistent with these previous reports (Table 7). From the results of our series, significance of regional lymph node irradiation seemed to be still undetermined. However, it was at least speculated that progression to multiple myeloma or distant metastases was observed more frequently and seemed to be much more important than regional lymph nodes (Table 4). The subject whether, in any subgroup of plasmacytoma of the head and neck, single modality of radiotherapy could achieve comparable or favorable treatment outcome should be discussed and further investigated. For example, overall survival rate of a subgroup consisted of 20 cases treated with radiotherapy, without surgery, and whose tumor sizes were less than 3 cm were almost similar to those of all 67 cases with or without surgery (5-year OS: 76% vs. 73%; and 10-year OS: 51% vs. 56%, respectively) (data not shown). Therefore, a single modality of radiotherapy might be applied if a tumor

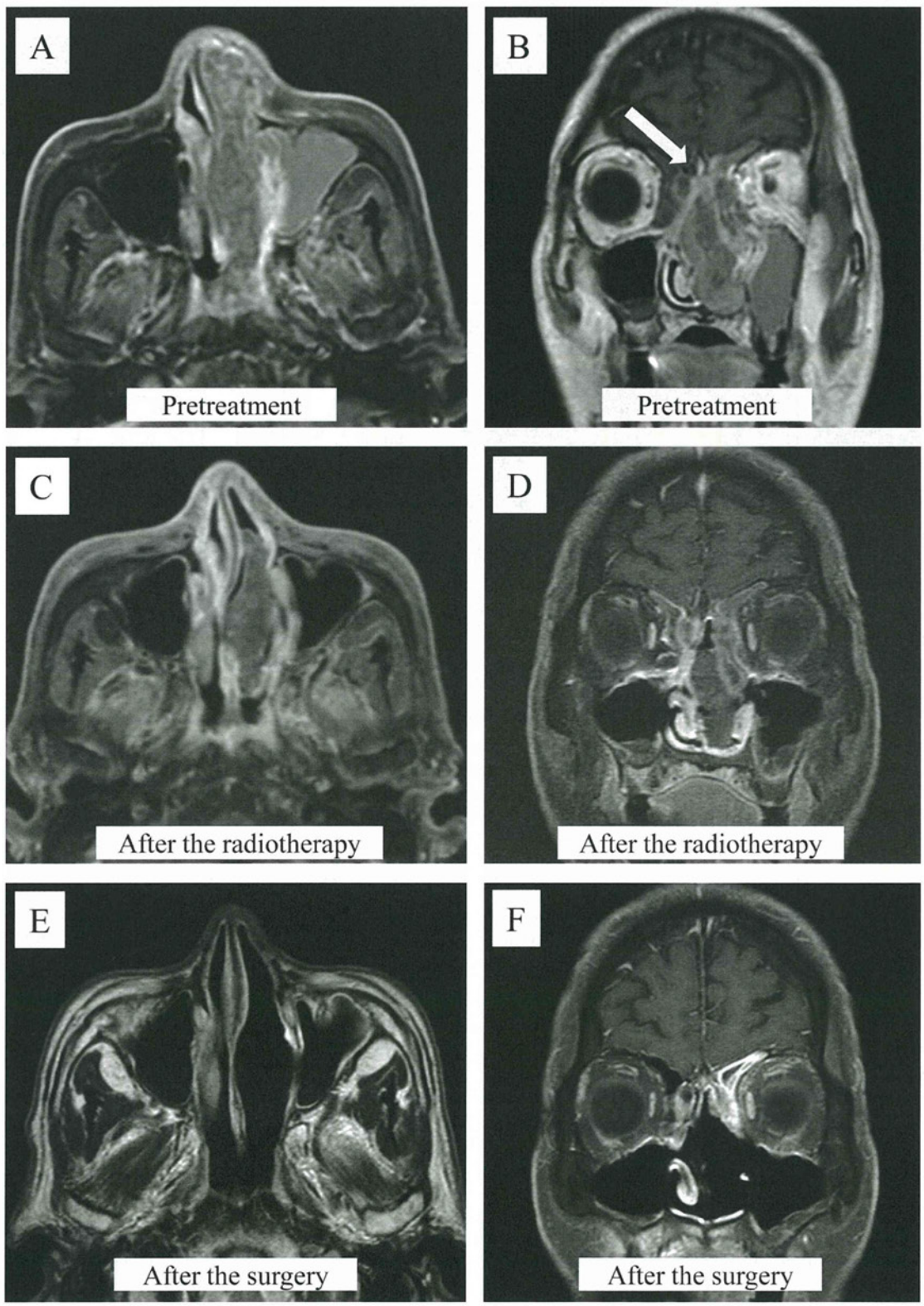

Fig. 6. Magnetic resonance imaging (MRI) of the 70-year-old male patient treated with the radiotherapy followed with the surgery. (A) Pretreatment images of the extramedullary plasmacytoma of the head and neck (EMP) located in the nasal cavity extended to the paranasal cavity. (B) A coronal image of MRI showing an invasion of the base of the skull. (C, D) Axial and coronal images of the residual tumor at the concha nasalis media shrunk after the radiotherapy. (E, F) Images of nasal and paranasal cavities after the surgical removal.

size was less than 3 cm. Although local controllability by either a single modality of radiotherapy or a combination of radiotherapy and surgery seemed to be satisfying, it might be discussed whether the local controllability could be truly led to prolong OS of the disease or not. In this study, population who received chemotherapy was small, and it was difficult to evaluate the efficacy of the chemotherapy. Further investigation, for example, into the significance of radiotherapy combined with chemotherapy might be evaluated. On the contrary, with using recent technological advances such as intensity-modulated radiotherapy (IMRT), image-guided radiotherapy, IGRT, or particle therapy, morbidities might be reduced compared with the morbidities of this study treated by conformal X-ray beams. Employment of such modalities might be recommended in the recent future.

Progression to multiple myeloma is also important for the outcome of solitary EMP. Unlike SPB, which progresses to disseminated disease in approximately 60% of cases, solitary EMP has a better prognosis, with 8–44% of patients developing multiple myeloma (1, 2, 4, 6, 9, 25, 27, 28, 32, 38–41). In our series, although 12% of patients developed MM (with an average time to myeloma development of 17 months), 18% of patients experienced distant metastases but were not diagnosed with progression to MM. In the literature, progression to multiple myeloma usually occurs within 2 years of the initial diagnosis, but has occurred up to 15 years later, indicating the need for long-term follow-up of patients (4, 6, 28, 39, 41, 42). As shown in the Table 4, there were only 1 patient who was treated to primary tumor site that experienced a regional lymph node recurrence. Therefore, it was still difficult to answer the question whether regional lymph nodes should be included in the radiation field form our series. However, significance of regional lymph node irradiation seemed to be undermined, because our series included various primary sites, various tumor size, and inhomogeneous total dose. Therefore, further larger scale investigation might be needed. Although the results of our series show a rather small percentage of patients developing MM, longer and careful follow-up observation might be needed.

The role for surgery in the treatment of EMPHN is undetermined. Alexiou *et al.* (7) compared the outcomes of EMP patients treated with surgery alone, radiotherapy alone, or combined surgery and radiotherapy in a detailed and large-scale review. Most of the patients were treated with surgery alone (56%) or a combined-modality treatment (20%), and only 11% were treated with radiotherapy alone. Overall and recurrence-free survival rates were best in those treated with combined therapy ($p = 0.0027$). The authors concluded that patients with plasmacytoma localized to the upper aerodigestive tract benefit from a combined approach. On the contrary, there are some criticisms of the analysis, because the review included patients from a long period (almost a century, 1905–1997), and appropriate radiotherapy might not have been available in any meaningful form for at least half of this period. In the guidelines regarding this disease published by Soutar *et al.* (35), it is recommended that radical surgery should be avoided in EMPHN. In the same report, complete surgical removal was suggested to be considered for solitary EMP at other sites if feasible. Bachar *et al.* (41) demonstrated that patients with involved surgical margins should receive adjuvant radiotherapy. However, no recommendation for adjuvant radiotherapy should be made for patients with negative margins who have undergone complete surgical excision. The authors reported that they found a similar local recurrence rate for patients treated with either radiation or surgery alone (12.5%). They also indicated that complete surgical excision is often not possible, especially in the upper aerodigestive tract, because adjacent vital organ structures may preclude radical intervention. For such patients, either radiotherapy followed by surgery, if needed, or surgical excision followed by radiotherapy is recommended. In our series, a group of 19 patients who received surgery followed by postoperative radiotherapy and 4 patients who received radiotherapy and surgery showed significantly better overall survival. This result indicates that combining radiotherapy with surgery might be less invasive and may represent an optimal strategy for treating EMPHN.

Some authors believe that EMP and multiple myeloma are different phases of the same disease process (43), whereas others believe that they are different diseases (44). If solitary EMP is an initial stage of MM, chemotherapy might play a more important role in management of the disease. However, in the literature and in our series, progression to MM occurred in a rather small proportion of patients. There is no published evidence on the role of adjuvant chemotherapy in the treatment of SEP, although it may have a role in selected high-risk patients. Susnerwala *et al.* (9) reported a higher failure rate in "high-grade" tumors using the MM grading criteria of Bartl *et al.* (36). Tsang *et al.* (29) and Holland *et al.* (25) suggested that patients with tumors >5 cm are at higher risk of failure. The UK Myeloma Forum (35) has suggested that chemotherapy is considered for EMP in the following cases: patients with tumors larger than 5 cm, patients with high-grade tumors, patients with refractory and/or relapsed disease, and patients with MM.

In conclusion, radiotherapy was effective and safe for patients with EMPHN. Radiotherapy combined with surgery produced a better outcome in terms of survival. These findings should be confirmed using further investigations with larger numbers of patients with EMPHN.

REFERENCES

1. Knowling MA, Harwood AR, Bergsagel DE. Comparison of extramedullary plasmacytomas with solitary and multiple plasma cell tumors of bone. *J Clin Oncol* 1983;1:255–262.
2. Mayr NA, Wen BC, Hussey DH, *et al.* The role of radiation therapy in the treatment of solitary plasmacytomas. *Radiother Oncol* 1990;17:293–303.

3. Shih LY, Dunn P, Leung WM, *et al.* Localised plasmacytomas in Taiwan: Comparison between extramedullary plasmacytoma and solitary plasmacytoma of bone. *Br J Cancer* 1995;71:128–133.
4. Liebross RH, Ha CS, Cox JD, *et al.* Clinical course of solitary extramedullary plasmacytoma. *Radiother Oncol* 1999;52:245–249.
5. Perez CA. Unusual nonepithelial tumors of the head and neck. In: Perez CA, Brady LW, editors. Principles and practice of radiation oncology. 3rd ed. Philadelphia: Lippincott Raven Publishers; 1997. p. 1116–1117.
6. Alexiou C, Kau RJ, Dietzfelbinger H, *et al.* Extramedullary plasmacytoma: Tumor occurrence and therapeutic concepts. *Cancer* 1999;85:2305–2314.
7. Wax MK, Yun KJ, Omar RA. Extramedullary plasmacytomas of the head and neck. *Otolarygol Head Neck Surg* 1993;109:877–885.
8. Brinch L, Hannisdal E, Foss Abrahamsen A, *et al.* Extramedullary plasmacytomas and solitary plasma cell tumours of bone. *Eur J Haematol* 1990;44:131–134.
9. Susnerwala SS, Shanks JH, Banerjee SS, *et al.* Extramedullary plasmacytoma of the head and neck region: clinicopathological correlation in 25 cases. *Br J Cancer* 1997;75:921–927.
10. Galieni P, Cavo M, Pulsoni A, *et al.* Clinical outcome of extramedullary plasmacytoma. *Haematologica* 2000;85:47–51.
11. Cavanna L, Fornari F, Civardi G, *et al.* Extramedullary plasmacytoma of the testicle. Sonographic appearance and ultrasonically guided biopsy. *Blut* 1990;60:328–330.
12. Rubin J, Johnson JT, Killeen R, *et al.* Extramedullary plasmacytoma of the thyroid associated with a serum monoclonal gammopathy. *Arch Otolaryngol* 1990;116:855–859.
13. Matsumiyama K, Kanayama Y, Yamaguchi S, *et al.* Extramedullary plasmacytoma (EMP) of urinary bladder. *Urology* 1992;40:67–70.
14. Nonamura A, Mizukami Y, Shimizu J, *et al.* Primary extramedullary plasmacytoma of the lung. *Inter Med* 1992;231:1396–1400.
15. Wong KF, Chan JK, Li LP, *et al.* Primary cutaneous plasmacytoma—report of two cases and review of the literature. *Am J Dermatopathol* 1994;16:391–397.
16. Adkins JW, Shields JA, Shields CL, *et al.* Plasmacytoma of the eye and orbit. *Int Ophthal* 1996;20:339–343.
17. Fischer C, Terpe HJ, Weidner W, *et al.* Primary plasmacytoma of the testis. Case report and review of the literature. *Urologia Internationalis* 1996;56:263–265.
18. Tuting AU, Bork K. Primary plasmacytoma of the skin. *J Am Acad Der* 1996;34:386–390.
19. Emery JD, Kennedy AW, Tubbs SR, *et al.* Plasmacytoma of the ovary: A case report and literature review. *Gynaecol Oncol* 1999;73:151–154.
20. Muscardin LM, Pulsoni A, Cerroni L. Primary cutaneous plasmacytoma: Report of case with review of the literature. *J Am Acad Der* 2000;43:962–965.
21. di Chiara A, Losito S, Terracciano L, *et al.* Primary plasmacytoma of the breast. *Arch Pathol Lab Med* 2001;125:1078–1080.
22. Dimopoulos MA, Kiamouris C, Moulopoulos LA. Solitary plasmacytoma of bone and extramedullary plasmacytoma. *Hematol Oncol Clin North Am* 1999;13:1249–1257.
23. Hu K, Yahalom J. Radiotherapy in the management of plasma cell tumors. *Oncology* 2000;14:101–111.
24. Harwood AR, Knowling MA, Bersagel DE. Radiotherapy of the extramedullary plasmacytoma of the head and neck. *Clin Radiol* 1981;32:31–36.
25. Holland J, Trenkner DA, Wasserman TH, *et al.* Plasmacytoma: Treatment results and conversion to myeloma. *Cancer* 1992;69:1513–1517.
26. Soesan M, Paccagnella A, Chiarion-Sileni V, *et al.* Extramedullary plasmacytoma: Clinical behaviour and response to treatment. *Ann Oncol* 1992;3:51–57.
27. Kapadia SB, Desai U, Cheng VS. Extramedullary plasmacytoma of the head and neck: a clinicopathologic study of 20 cases. *Medicine* 1982;61:317–329.
28. Miller FR, Lavertu P, Wanamaker JR, *et al.* Plasmacytomas of the head and neck. *Otolaryngol Head Neck Surg* 1998;119:614–618.
29. Tsang RW, Gospodarowicz MK, Pintilie M, *et al.* Solitary plasmacytoma treated with radiotherapy: impact of tumor size on outcome. *Int J Radiat Oncol Biol Phys* 2001;50:113–120.
30. Jyothirmayi R, Gangadharan VP, Nair MK, *et al.* Radiotherapy in the treatment of solitary plasmacytoma. *Br J Cancer* 1997;70:511–516.
31. Bolek TW, Marcus RB, Mendenhall NP. Solitary plasmacytoma of bone and soft tissue. *Int J Radiat Oncol Biol Phys* 1996;36:329–333.
32. Tournier-Rangeard L, Lapeyre M, Graff-Caillaud P, *et al.* Radiotherapy for solitary extramedullary plasmacytoma in the head-and-neck region: A dose greater than 45 Gy to the target volume improves the local control. *Int J Radiat Oncol Biol Phys* 2006;64:1013–1017.
33. Mendenhall CM, Thar TL, Million RR. Solitary plasmacytoma of bone and soft tissue. *Int J Radiat Oncol Biol Phys* 1980;6:1497–1501.
34. Creach KM, Foote RL, Neben-Wittich MA, *et al.* Radiotherapy for extramedullary plasmacytoma of the head and neck. *Int J Radiat Oncol Biol Phys* 2009;73:789–794.
35. Soutar R, Lucraft H, Jackson G, *et al.* Guidelines on the diagnosis and management of solitary plasmacytoma of bone and solitary extramedullary plasmacytoma. *Br J Haematol* 2004;124:717–726.
36. Bartl R, Frisch B, Fateh-Moghadam A, *et al.* Histologic classification and staging of multiple myeloma. A retrospective and prospective study of 674 cases. *Am J Clin Pathol* 1987;87:342–355.
37. Chao MW, Gibbs P, Wirt A, *et al.* Radiotherapy in the management of solitary extramedullary plasmacytoma. *Intern Med J* 2005;35:211–215.
38. Greenberg P, Parker RG, Fu YS, *et al.* The treatment of solitary plasmacytoma of bone and extramedullary plasmacytoma. *Am J Clin Oncol* 1987;10:199–204.
39. Michalaki VJ, Hall J, Henk JM, *et al.* Definitive radiotherapy for extramedullary plasmacytomas of the head and neck. *Br J Radiol* 2003;76:738–741.
40. Strojan P, Soba E, Lamovec J, *et al.* Extramedullary plasmacytoma: Clinical and histopathologic study. *Int J Radiat Oncol Biol Phys* 2002;53:692–701.
41. Bachar G, Goldstein D, Brown D, *et al.* Solitary extramedullary plasmacytoma of the head and neck long-term outcome analysis of 68 cases. *Head Neck* 2008;30:1012–1019.
42. Bush SE, Goffinet DR, Bagshaw MA. Extramedullary plasmacytoma of the head and neck. *Radiology* 1981;140:801–805.
43. Batsakis JG, Fries GT, Goldman RT, *et al.* Upper respiratory tract plasmacytoma. *Arch Otolaryngol* 1964;79:613–618.
44. Dolin S, Dewar JP. Extramedullary plasmacytoma. *Am J Pathol* 1956;32:83–103.

CRYSTAL GROWTH & DESIGN

Article

pubs.acs.org/crystal

Surfactant-Assisted Hydrothermal Synthesis of Water-Dispersible Hafnium Oxide Nanoparticles in Highly Alkaline Media

Ameneh Sahraneshin,[†,‡] Shunsuke Asahina,[§] Takanari Togashi,[△] Varu Singh,[⊥] Seiichi Takami,[‡] Daisuke Hojo,[∥] Toshihiko Arita,[‡] Kimitaka Minami,[⊥] and Tadafumi Adschiri*[,‡,∥,⊥]

[†]Graduate School of Engineering, Tohoku University, 6-6 Aramaki Aza Aoba, Aoba-ku, Sendai 980-8579, Japan

[‡]Institute of Multidisciplinary Research for Advanced Materials, Tohoku University, 2-1-1 Katahira, Aoba-ku, Sendai 980-8577, Japan

[§]JEOL Ltd., SM Business Unit, 1-2 Musashino 3-Chome, Akisima, Tokyo 196-8558, Japan

[∥]World Premier International Research Center-Advanced Institute for Materials Research, Tohoku University, 2-1-1 Katahira, Aoba-ku, Sendai 980-8577, Japan

[⊥]New Industry Creation Hatchery Center, Tohoku University, 6-6-10 Aramaki Aza Aoba, Aoba-ku, Sendai 980-8579, Japan

[△]Department of Material and Biological Chemistry, Faculty of Science, Yamagata University, 1-4-12 Kojirakawa-machi, Yamagata 990-8560, Japan

Supporting Information

ABSTRACT: Hafnium oxide nanoparticles were synthesized via a short-duration (10 min) hydrothermal reaction. The reaction was found to produce three differently shaped nanoparticles: flower-like nanostructures (20 nm diameter), polycrystalline nanoagglomerates (25 nm diameter), and water-dispersible single nanoparticles (4 nm diameter). The mechanisms by which these different shapes form were then investigated by examining the effects of precursor alkalinity and the presence of an organic capping agent. The synthesized water-dispersible nanoparticles showed a very high affinity for water-soluble polymers, thus demonstrating their potential for fabrication of transparent nanocomposite films.

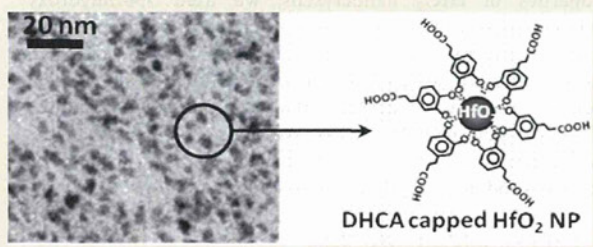

1. INTRODUCTION

Since the last two decades, high refractive index nanocomposite materials have attracted tremendous academic and industrial attention, owing to their novel tunable properties and wide range of applications such as fabrication of lenses, reflectors, optical waveguides, optical adhesives, and antireflection films.[1−6] The most commonly used NPs for the above-mentioned applications include ZnS (n = 2.36),[3] ZrO_2 (n = 2.20),[4] TiO_2 (anatase, n = 2.45; rutile, n = 2.70),[5] and PbS (n = 4.20).[6] For nanoparticles (NPs) to succeed in these applications, the following properties are critical: (1) optical transparency, (2) high dispersibility in the dispersion media, and (3) uniform and stable dispersibility in the matrix. Relevant factors that determine these properties include NP size, shape, and surface properties.

Quiet recently, hafnium oxide NPs is proposed as a high refractive index material with n = 2.9.[7,8] Compared to the previously reported candidates, in addition to its high refractive index, hafnium oxide NPs have other advantages such as excellent physical and chemical stability and optical transparency.

So far, various methods have been reported for synthesizing HfO_2 NPs, including sol−gel, solvothermal, hydrothermal, and microwave−hydrothermal methods.[9−12] Of these, only a limited number of reports claim the capability to control NP size, shape, and surface properties. A known effective way to tune NP size and shape and to prevent aggregation is to incorporate organic reagents in the reaction medium as capping ligands or shape-determining agents that control NP surface energy.[13−29] Similarly, an effective method to tune NP surface properties is to hybridize organic molecules on the NP surface, thereby making the NP compatible with the dispersion medium. For example, Tang et al. synthesized HfO_2 nanocrystals via reaction of hafnium isopropoxide with hafnium halides in the presence of trioctylphosphine oxide (TOPO) as solvent at 340 °C.[13] Similarly, Tirosh and Gil used the same procedure but with 1-octadecene as the organic solvent in the presence of oleylamine as an additional capping agent to synthesize HfO_2 nanorods.[14] Finally, Buha et al. used a sol−gel procedure based on the solvothermal reaction of hafnium chloride with benzyl alcohol as the solvent.[15] These researchers successfully synthesized small-size HfO_2 NPs, but unfortunately, their reported methods require large amounts of organics, thus risking, particularly in the case of the solvothermal method, considerable ecological harm. Moreover, NPs synthesized via these methods tend to have hydrophobic

Received: April 27, 2012
Revised: September 26, 2012
Published: October 1, 2012

   dx.doi.org/10.1021/cg3005739 | Cryst. Growth Des. 2012, 12, 5219−5226

surfaces. Therefore, for applications that require water-dispersible NPs such as for loading in water-soluble polymers and immersion fluids, an additional ligand-exchange process is required to produce NPs with hydrophilic surfaces.[30,31]

A promising green process has recently been suggested for synthesizing organic–inorganic hybrid metal–oxide nanocrystals with narrow size distributions: reaction in a medium of high-temperature, high-pressure near-critical to supercritical water.[16−24] The reasoning for this approach is that the dielectric constant of high-temperature water is close to that of polar organic solvents (10–20). Hence, organic reagents should be miscible in high-temperature water and react effectively with the NP surface, enabling control of NP surface properties.

In our previous paper, we reported the rapid hydrothermal synthesis of organic surface modified HfO_2 NPs with hydrophobic surface character.[32] We showed how to control the size, morphology, and surface properties of HfO_2 NPs by changing the state of water (subor supercritical condition) and type of organic functional groups. Herein, we report the use of the same approach (i.e., using near critical water as the reaction medium) to achieve the first simple synthesis of highly water dispersible, uniformly sized HfO_2 NPs. To control the surface properties of HfO_2 nanocrystals, we used 3,4-dihydroxy hydrocinnamic acid (DHCA) as a bifunctional organic grafting agent. One of the agent's functional groups forms a chemical bond on the NP surface; its remaining unbounded functional groups serve to make the NP surface hydrophilic and thus the NPs dispersible in polar media. We intend to investigate the mechanism by which different shaped NPs are formed by observing the effect of different reaction conditions.

2. EXPERIMENTAL SECTION

Starting materials were hafnium tetrachloride, $HfCl_4$ [99.99%, Wako Chemicals], and potassium hydroxide, KOH [99.99%, Wako Chemicals]. A precursor solution was prepared by dissolving 0.160 g of $HfCl_4$ in 10.0 mL of deionized water. KOH aqueous solution (0.20 M, 10.0 mL) was added dropwise to the precursor solution with continuous stirring, resulting in the formation of hafnium hydroxide, $Hf(OH)_4$, according to the following stoichiometries:[33,34]

$$HfCl_4 + 2H_2O \rightarrow Hf(OH)_2Cl_2 + 2HCl$$

$$Hf(OH)_2Cl_2 + 2KOH \rightarrow Hf(OH)_4 + 2KCl$$

The white $Hf(OH)_4$ solid thus formed was purified by two cycles of centrifugation and decantation using deionized water to remove Cl^- ions, which can otherwise corrode the reactors. The precipitate was dispersed in KOH solutions of different molarities (0.0, 0.10, 0.20, 0.30, 0.40, and 0.50 M) to reach a final volume of 10.0 mL. The Hf ion concentration in the final solution was 0.050 M.

Pressure-resistant tube reactors (SUS 316, inner volume 5.0 mL) were used to synthesize HfO_2 NPs. The reactor was filled with a specific amount of DHCA [98%, Aldrich Chemistry] (0.045–0.135 g), loaded with 2.50 mL of precursor solution, capped tightly, and placed in an electric furnace (preheated to 350 °C). The concentration of DHCA in the reaction mixture varied from 0.10 to 0.30 M; hence, the molar ratio of DHCA to Hf varied from 2:1 to 6:1. Reaction was allowed to proceed for 10 min, and then terminated by quenching the reactor in a room-temperature water bath. The products were collected using 3 mL of water and purified by three cycles of centrifugation and decantation with a mixture of ethanol and water (volume ratio 6:1). The products were dispersed in water and kept overnight. During this period, bigger/unmodified NPs precipitated. The supernatant was separated and freeze-dried under vacuum overnight.

Powder X-ray diffraction (XRD) patterns of the products were collected using an X-ray diffractometer (Rigaku Ultima IV) with Cu–Kα radiation in a $2\theta-\theta$ setup; the 2θ angle was scanned from 15° to 80°. JADE software (MDI JADE 7 Materials Data XRD Pattern Processing, Identification, and Quantification) was used to evaluate/analyze the XRD patterns. Product size and morphology were analyzed using a transmission electron microscope (TEM, Hitachi H7650) at an accelerating voltage of 100 kV. Fourier-transform infrared (FTIR) spectra were acquired using a JASCO FT/IR-680 spectrometer to evaluate the presence of DHCA molecules on the NP surface; a KBr palette was used for sample preparation. Transmission IR spectra were collected over the range 400–4000 cm^{-1}. The amount of DHCA molecules attached to the NPs was evaluated by thermogravimetric analysis (TGA) on a TGDTA T8120 (Rigaku, Japan) under a constant flow of Ar gas in the temperature range 20–800 °C with a ramp rate of 10 °C/min.

3. RESULTS AND DISCUSSION

3.1. Effect of KOH Concentration on NP Crystallization. Figure 1 shows XRD patterns of HfO_2 NPs synthesized in the presence of DHCA (0.10 M) and different KOH concentrations. Comparison of the obtained patterns with the standard JCDPS patterns for different crystal phases of HfO_2 reveals that all NPs that are formed have the monoclinic HfO_2 crystal structure. Increasing KOH concentration results in sharper peaks, indicating that KOH improves NP crystallization. KOH also affects the intensity ratio between peaks. Table 1 shows peak areas of the XRD patterns for the two most prominent planes, (111) and (022), among NPs synthesized with different KOH concentrations.

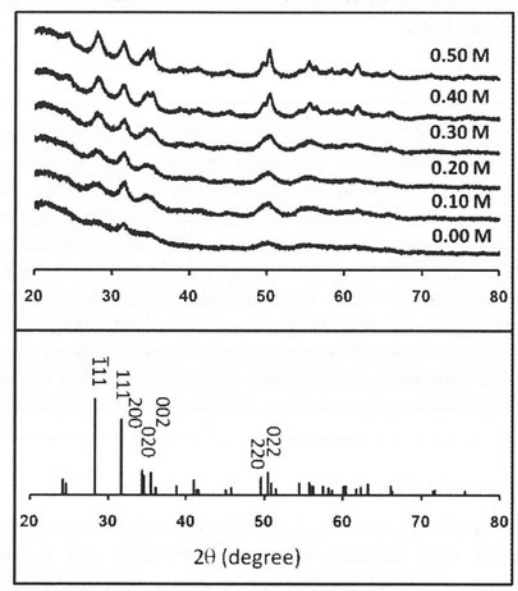

Figure 1. XRD patterns of HfO_2 NPs. (top) Obtained patterns of HfO_2 NPs synthesized with 0.10 M DHCA and various KOH concentrations. (bottom) JCPDS pattern of monoclinic HfO_2 (JCPDS code: 34-0104).

Figure 2 shows a plot of the ratio of the areas under the XRD peaks along (111) and (022) planes versus KOH concentration. With increasing KOH concentration, the ratio decreases and approaches 1, suggesting anisotropic nanocrystal growth at smaller KOH concentrations. At low KOH concentrations (0.10 and 0.20 M KOH), the (111) peak is

dx.doi.org/10.1021/cg3005739 | Cryst. Growth Des. 2012, 12, 5219–5226

Table 1. Peak Area of the Two Most Prominent Peaks ([111] and [022]) and Morphology of HfO_2 NPs Synthesized with 0.1 M DHCA and Various KOH Concentrations

	peak intensity in JCPDS pattern 34-0104		area under the peak			
KOH concentration (M)	[111]	[022]	[111]	[022]	area ratio [111]/[022]	morphology
0.10	1.0	0.78	21114	8428	2.505	needle
0.20			14910	7255	2.055	oval
0.30			16273	13796	1.179	spherical
0.40			20974	21612	0.970	spherical
0.50			24427	21464	1.138	spherical

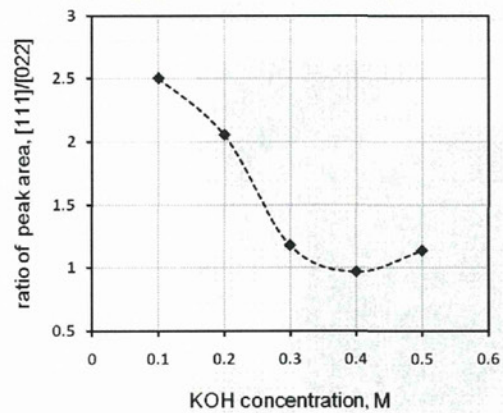

Figure 2. Plot of peak-area ratio for the most prominent XRD peaks (those corresponding to the (111) and (022) planes) versus KOH concentration.

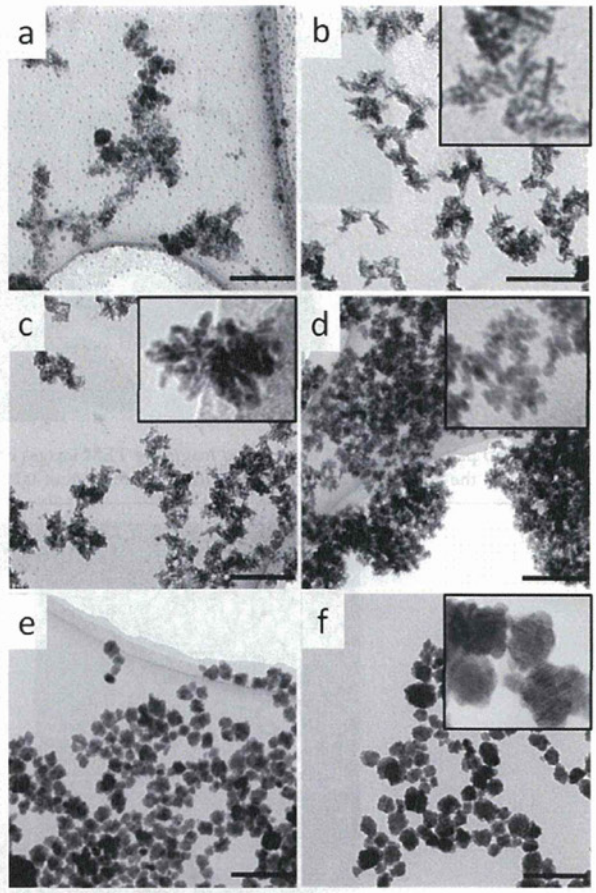

Figure 3. TEM images and inset magnified images of HfO_2 NPs synthesized with 0.10 M DHCA and various KOH concentrations: (a) 0.00, (b) 0.10, (c) 0.20, (d) 0.30, (e) 0.4, and (f) 0.50 M. Scale bars = 100 nm.

more intense than the peaks for the other planes, indicating faster crystal growth along the [111] direction. At higher KOH concentrations (0.30 to 0.50 M KOH), the peaks for the other planes grow and all peak intensities become essentially the same as those of the standard XRD pattern for monoclinic HfO_2 (JCPDS pattern 34-0104).

Figure 3 shows TEM images that reveal the morphology of the produced NPs. Before the addition of KOH to the reaction mixture, the NPs lack a clear shape (Figure 3a). With increasing KOH concentration, small primary particles form and then aggregate into nanoclusters (Figures 3b–d). At 0.10 M KOH (Figure 3b), the primary particles are needle-shaped. At 0.20 M KOH (Figure 3c), they become more oval-shaped. Both needle-shaped and oval-shaped primary NPs are consistent with the observed XRD patterns described above, indicating that anisotropic nanocrystal growth occurs under these two alkaline conditions. At 0.30 M KOH (Figure 3d), the primary particles become spherical-shaped, with a diameter of 4 nm. Finally, at 0.40 and 0.50 M KOH (Figures 3e,f), the primary particles become dense flower-like nanostructures comprising spherical NPs.

The strong effect of the precursor pH on the NP morphology and crystal structure has been reported previously.[35−38] In almost all the references on the pH controlled crystal growth, it is mainly postulated that the pH of the starting solution changes the growth rate of crystallographic planes with different surface energies and leads the formation of differently shaped nanostructures. However, no generalized conclusion has been proposed yet. Jia et al. proposed that the pH of the reaction mixture can control the dissociation rate of the precursor, which significantly affects the supply of metal ions in the reaction environment and thus the growth rate of the metal-oxide nanocrystals.[36] Ren et al.[37] and Zhang et al.[38] speculated that OH^- group as an adsorbing ligand could be served as a surface modifier and control the crystal growth via a preferential manner under some certain alkaline conditions. Ren et al.[37] observed such preferential behavior under low pH conditions; whereas they obtained spherical particles under high pH conditions suggesting the same crystal growth in almost all directions under highly alkaline conditions.

Other evidence of the effect of pH on crystallization has also been reported previously. For example, Stefanic et al. found that hydrothermal crystallization of HfO_2 is a pH-dependent process, with crystallization proceeding much more slowly in a neutral pH medium than in an acidic or alkaline medium.[39] Such a trend in crystallization versus pH has also been reported for zirconium oxide, which has a crystal system similar to that of hafnium oxide.[40−42]

In summary, our XRD and TEM results show that, at low KOH concentrations (0.10 and 0.20 M), the NP growth rate is

dx.doi.org/10.1021/cg3005739 | Cryst. Growth Des. 2012, 12, 5219–5226

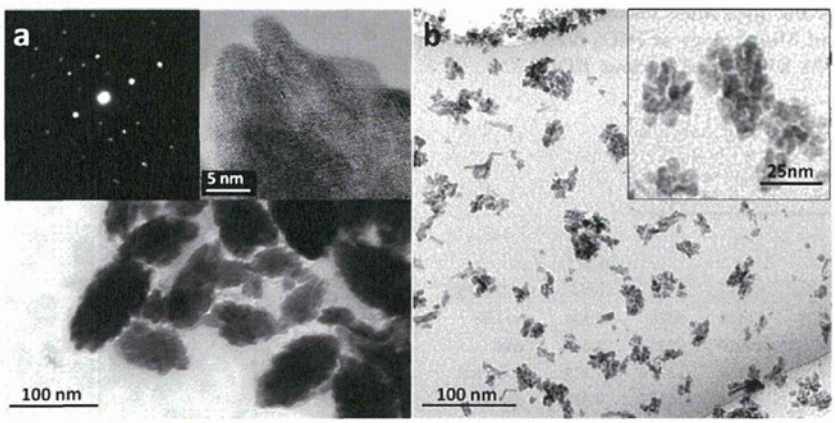

Figure 4. ED patterns, HRTEM images, and magnified TEM images of HfO_2 NPs synthesized under various conditions: (a) in the presence of 0.50 M KOH and the absence of organics and (b) in the presence of 0.20 M KOH and the organic *t*-butyl cathecol (0.20 M).

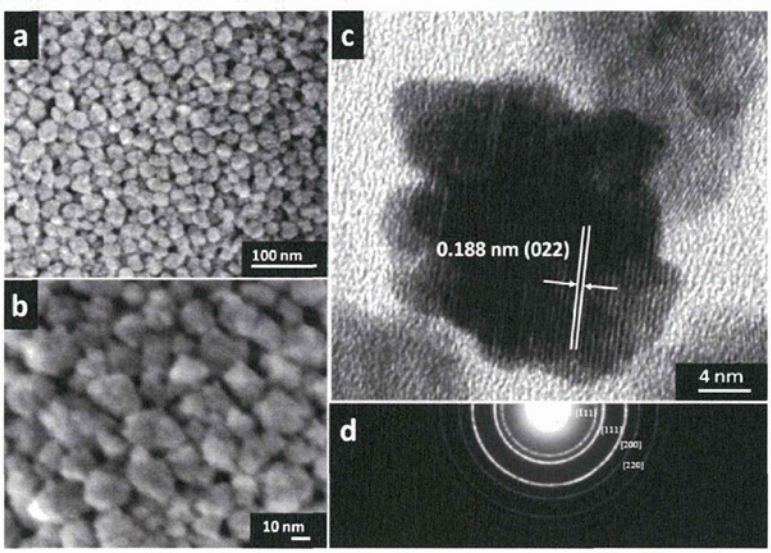

Figure 5. Flower-like HfO_2 NPs corresponding to Figure 2f: (a,b) HRSEM images, (c) HRTEM image, and (d) ED pattern.

higher in the (111) plane than in the other planes, resulting in the formation of needle-shaped NPs. With increasing KOH concentration, the growth rate of (111) plane was controlled by OH^- ions, resulting in the formation of spherical-shaped NPs. The origin of such effect is that the (111) plane of HfO_2 is a quasi polar surface, that is, O–Hf–O layer repeated to the [111] direction. Therefore, this plane is unstable and has higher surface energy. When OH concentration becomes large, capping of the (111) plane by OH^- ion and/or shielding of surface charge by concentrated charged ions slowed the growth rate of the (111) plane.

Nanoparticle size is strongly influenced by the nucleation rate of nanocrystals, which is also a strong function of metal oxide solubility in the reaction medium. When the solubility of metal oxides decreases, their degree of supersaturation raises, and therefore, they precipitate in the reaction medium faster. This leads the increase of the nucleation rate and consequently formation of more crystal nuclei at the time corresponding to the crystallization of smaller sized NPs. Alkalinity of the reaction mixture is a keen parameter to govern the solubility of metal oxide. In the present case, based on the magnified TEM images, it was observed that, in the beginning by increasing the KOH concentration to 0.10, 0.20, and 0.30 M, the particle dimensions reduced from needle to oval to nanosphere, respectively. This reducing trend in the dimensions of nanoparticles shows a decrease in the solubility of HfO_2. After increasing the KOH concentration to more than 0.30 M, the nanoparticles size drastically increased; that shows an increase in the solubility of HfO_2 nanocrystals under higher alkalline conditions, leading the enhanced Ostwald ripening. Therefore, the higher KOH concentration resulted in shaper XRD peaks and larger nanocrystals (formation of dense flower-like nanostructures).

3.2. Relative Effects of KOH Concentration and DHCA on NP Nanoassembly. At high KOH concentrations (0.40 and 0.50 M, Figure 3e,f), the reaction produces dense flower-like nanostructures comprising smaller primary spherical NPs. Similar phenomena involving the formation of nanostructures composed of agglomerated NPs in the presence of multifunctional modifiers such as DHCA or dicarboxylic acids have been reported previously.[18,43,44] For example, Togashi et al.[18] and Takami et al.[43] have reported that such multifunctional organic

dx.doi.org/10.1021/cg3005739 | *Cryst. Growth Des.* 2012, 12, 5219–5226

molecules can act as linkers between two primary particles. Other researchers have reported the formation of nanostructures composed of primary particles in alkaline media in the presence[45,46] and even the absence[36,38,47] of organic capping agents. For example, Eliziario et al. have reported the formation of rice-shaped HfO_2 nanostructures composed of small primary particles in the absence of any organic molecules but in a highly alkaline medium;[47] however, they did not mention the effect of the alkalinity of the reaction medium on product morphology.

We surmise that, in addition to the presence of DHCA, high alkalinity of the reaction medium is important for controlling NP assembly in our experiment. To determine the relative importance of the two factors, the presence of DHCA and the alkalinity of the precursor solution, for the formation of HfO_2 nanostructures, we repeated our experiment both in the absence of a modifier (specifically, the bifunctional modifier DHCA) and the presence of a monofunctional modifier.

Figure 4 shows images of NPs formed in the absence of a modifier and in the presence of a monofunctional modifier, but under the same reaction conditions. Reaction in the absence of a modifier gives cluster-like structures that are large (120 nm) and spindle-shaped, similar to the structures reported in ref 47 (Figure 4a). Reaction in the presence of the monofunctional modifier 4-*tert*-butylcatechol (*t*-BC), which has the same molecular structure as that of DHCA but lacks a carboxyl group, gives nanoagglomerates composed of approximately 5 nm spherical NPs (Figure 4b). These observations confirm that the multifunctionality of DHCA is not responsible for NP agglomeration in our case. However, the alkalinity of the reaction mixture plays a key role in determining the morphology of final structures. Comparison between TEM images and XRD patterns of the NPs synthesized under highly alkaline conditions (Figure 4a) with those synthesized in the absence of KOH and organic molecules (our previous paper[32]), which is illustrated in Figure S1 of Supporting Information, shows that, under highly alkaline conditions, formation of final products passes a completely different crystallization pathway. This is due to the drastic change in the solubility of HfO_2 under highly alkaline conditions, which strongly influences its precipitation–recrystallization process.

Our next aim was to investigate the crystallographic orientation of primary NPs in the flower-like nanostructures shown in Figure 3e,f. Figure 5 shows the habitus of a single nanoflower, observed by high-resolution SEM (HRSEM), high-resolution TEM (HRTEM), and electron diffraction (ED). The obvious regular parallel lattice fringes without any lattice mismatch (Figure 5c) demonstrated that the obtained nanoflowers were single-crystalline structures. The interplanar spacing was determined in approximately 0.188 nm, which corresponds to the {022} crystallographic planes. The position of rings in ED pattern (Figure 5d) was closely matching with the monoclinic $P2_1/a$ space group, using the HfO_2 unit cell parameters of JCPDS no. 34-0104, which confirms the XRD results on the formation of pure monoclinic phase. Figure S2 (of Supporting Information) shows the shape evolution of the nanoflowers as the reaction proceeds, as observed by TEM at short reaction times. By 1.5 min (Figure S1a, Supporting Information), ultrafine NPs form; by 2 min, some primary nanoparticles begin to grow; by 5 min, all products convert to well-formed nanoflowers.

3.3. Effect of DHCA Concentration on NP Shape. The presence of DHCA appears to limit NP growth and aggregation, as evidenced by the fact that the size of structures obtained in the presence of DHCA (Figure 3f) is considerably smaller than the size obtained in the absence of DHCA (Figure 4a). To investigate the effect of DHCA on the final product characteristics, we conducted experiments with different amounts of added DHCA in 0.50 M KOH as the reaction medium.

Figure 6 shows TEM images of the as-formed NPs. Figure S3 (Supporting Information) represents the XRD pattern of the

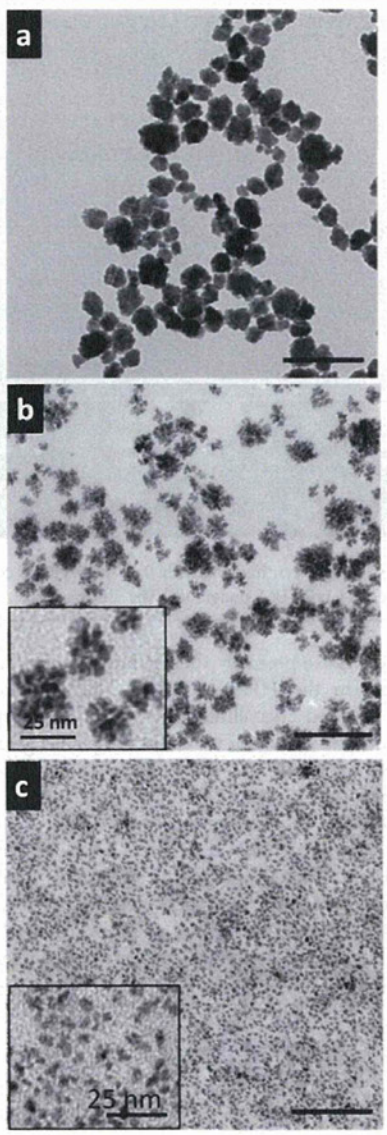

Figure 6. TEM images and inset magnified images of HfO_2 NPs synthesized with 0.50 M KOH and various DHCA concentrations: (a) 0.10, (b) 0.20, and (c) 0.30 M. Scale bars = 100 nm.

HfO_2 NPs synthesized with different concentrations of DHCA. All the patterns match with the standard XRD pattern for monoclinic HfO_2 (JCPDS pattern 34-0104). Increasing DHCA concentration from 0.10 to 0.20 M results in the formation of HfO_2 nanoagglomerates of approximately 25 nm in diameter. From Scherer's equation, we estimate the crystallite size to be 7.25 nm for each primary nanocrystal. The clear boundary

dx.doi.org/10.1021/cg3005739 | Cryst. Growth Des. 2012, 12, 5219–5226

between the primary nanocrystals, observed in the magnified TEM image (Figure 6b inset), reveals the polycrystallinity of the nanoagglomerates. Further increasing DHCA concentration to 0.30 M results in single separated NPs having diameter 4 nm. These results confirm the limiting role of DHCA molecules, as capping agent, on HfO_2 NP growth and agglomeration.

Figure 7 shows an HRTEM image and an ED pattern of NPs formed in the presence of a high concentration of DHCA (0.30 M), revealing more precisely their habitus. A clear lattice fringe can be seen in the HRTEM image, this indicates that the products had good crystallinity and were not amorphous. The measured distance between two adjacent planes gives a value of about 0.187 nm, which corresponds to the lattice spacing of {022} planes.

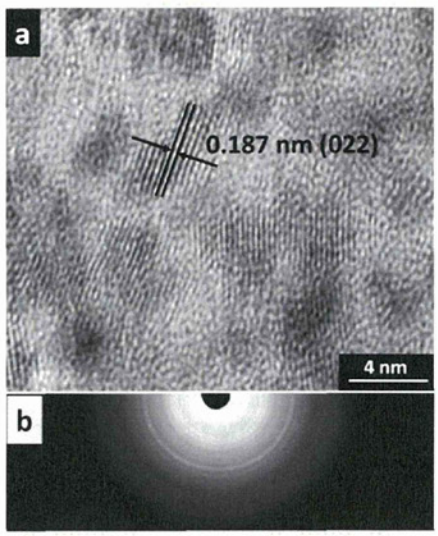

Figure 7. HfO_2 NPs synthesized with 0.30 M DHCA, corresponding to Figure 5c: (a) HRTEM image and (b) ED pattern.

Figure 8 shows FTIR spectra of DHCA, both free and coordinated on HfO_2 NPs. For free DHCA (Figure 8A), the main bands are assigned as follows: stretching vibrations of the aromatic ring ν(C−C)/ν(C=C) at 1597, 1527, and 1445 cm^{-1}; stretching vibrations of the phenolic group ν(C−OH) at 1265 and 1245 cm^{-1}; bending vibrations of the phenolic group δ(C−OH) at 1403, 1355, 1284, and 1167 cm^{-1}; stretching or bending vibrations of CO in COOH at 1265, 1245, 1230, and 1203 cm^{-1}; and stretching vibration of the carbonyl group ν(C=O) at 1675 cm^{-1}.[48,49] For DHCA adsorbed on the HfO_2 NP surface (Figure 8B), the positions of the vibration bands change; specifically, the bands at 1167, 1245, 1284, and 1355 cm^{-1} disappear and new bands at 1260 and 1492 cm^{-1} appear, suggesting chemical bonding of the phenolic groups on the NP surface. The presence of bands at around 1201 and 1630 cm^{-1}, assigned to vibrations of the unbounded carboxylic group, indicate the existence of unbounded carboxylic groups on the surface of HfO_2 NPs.[18,50] The surface immobilization of oxygen atoms of catechol group to form M−C−O bonding would definitely change the environment of the aromatic ring causing the shifting of its bands. In the FTIR spectra of the DHCA adsorbed on the NP surface, the band at 1560 cm^{-1} could be attributed to the stretching vibration of the aromatic ring, which is shifted from 1597 cm^{-1} to lower wavenumbers in this new environment.

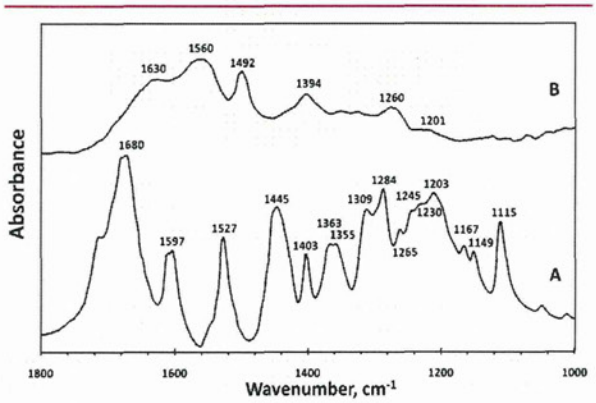

Figure 8. FTIR spectra: (A) neat DHCA and (B) HfO_2 NPs hybridized with DHCA.

We measured the density of DHCA molecules attached to the NP surface by TGA. Figure S4 (Supporting Information) shows plots of weight loss versus temperature for NPs synthesized in the presence of different DHCA concentrations. Subtracting the weight loss of samples synthesized in the absence of DHCA from that of samples synthesized in the presence of DHCA gives the following DHCA molecule weight percentages: 2.3 wt % for nanoflowers, 5.1 wt % for nanoagglomerates, and 10.9 wt % for single NPs. Weight loss of the synthesized NPs starts at approximately 320 °C and thus is presumably caused by the thermal decomposition of DHCA molecules attached to the NP surface. Furthermore, weight loss increases with increasing amounts of DHCA on the NP surface. We estimate the density of DHCA molecules on the surface of a single separated 4 nm NP to be approximately 2.0 molecules/nm^2 (the procedure used to estimate such value is explained in the Supporting Information).

3.4. Colloidal Dispersions of HfO_2 NPs. Incorporation of inorganic NPs into the polymeric matrixes to improve their optical properties is a new promising approach for the fabrication of high refractive index hybrid materials. To manipulate NPs for such applications, some important issues, however, should be considered: (i) NPs dispersed in nanocomposites can be detrimental to the optical performances of the basic polymer because of the loss of transmitted light by scattering. Highly filled nanocomposites with a large difference between the refractive indices of the matrix and the dispersed NPs can be readily transparent if the NPs are small enough (typically diameters of less than 25 nm).[51] (ii) The next challenging issue is to make uniform and durable dispersions of NPs in the host media; aggregation of NPs can drastically deteriorate the transparency of the nanocomposites.

Two properties are associated with stable, long-term (on the order of months) NP dispersibility in water: small diameter (4 nm) and the presence of unbounded carboxyl groups on the NP surface, making the surface hydrophilic. Figure 9 shows the dispersion of 2.0 wt % of synthesized HfO_2 NPs in water. These NPs exhibit high water dispersibility and thus are expected to show high affinity for water-soluble polymers, a desired property for the fabrication of polymeric nanocomposites. To investigate this issue, we dispersed HfO_2 NPs in a film composed of polyvinyl alcohol (PVA), a water-soluble polymer. (The protocol we used for the fabrication of naocomposite films is schematically represented in the Supporting Informa-

dx.doi.org/10.1021/cg3005739 | Cryst. Growth Des. 2012, 12, 5219−5226

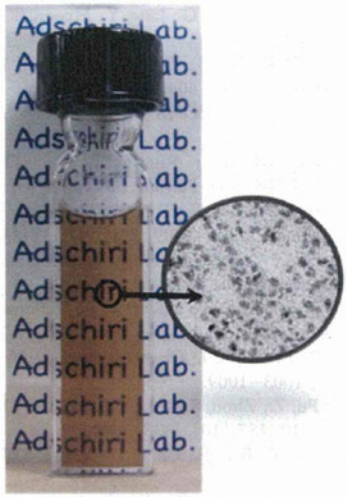

Figure 9. Dispersion of HfO_2 NPs (diameter 4 nm) synthesized with 0.30 M DHCA.

tion.) Figure 10 shows SEM and AFM images of the pure film and a nanocomposite film formed by dispersion of 50 wt % HfO_2 NPs in a PVA matrix. An SEM image of the composite film (Figure 10b) shows that the NPs are perfectly dispersed in the matrix, with almost no aggregation. An AFM image of the composite film (Figure 10d) shows that the surface roughness of the nanocomposite is around 7 nm, on the same order as the NP size, indicating that the NPs are uniformly dispersed in the matrix and not aggregated on the film surface. Although, the small size and perfect dispersibility in polymer matrix are the essential conditions to prove the applicability of our HfO_2 NPs for the fabrication of nanocomposite film, but to accomplish the study, it is highly desired to qualify the fabricated nanocomposite films by evaluating the functionalities of the prepared films such as their refractive index and optical transparency, which is the scope of our future paper.

4. CONCLUSIONS

We achieved the systematic hydrothermal synthesis of water-dispersible HfO_2 nanoparticles in 350 °C, 16 MPa water within a short reaction time of 10 min. We determined that the alkalinity of the precursor solution played an indispensible role on the crystallization of HfO_2 NPs. The strong effect of the reaction alkalinity on the solubility of HfO_2 crystal was addressed as the key factor for controlling the size and shape of the nanocrystals. By incorporating different amounts of 3,4-dihydroxy hydrocinnamic acid (DHCA) as a multifunctional capping agent, we succeeded to control the size of the final nanostructures in the range of 25 to 4 nm. DHCA molecules chemically bonded on the surface of NPs via their phenolic groups. The existence of unbounded carboxylic groups on the NPs surface enabled them to have high dispersibility in water and excellent affinity with water-soluble polymers. We expect these HfO_2 nanoparticles to be good candidates for the fabrication of high-refractive-index transparent nanocomposites. We would further investigate the fabricated nanocomposite film by measuring its refractive index and optical transparency.

■ ASSOCIATED CONTENT

Ⓢ Supporting Information

TEM images, XRD patterns, TGA curves, estimation of number of modifier molecules per area of NP surface, fabrication of nanocomposite films. This material is available free of charge via the Internet at http://pubs.acs.org.

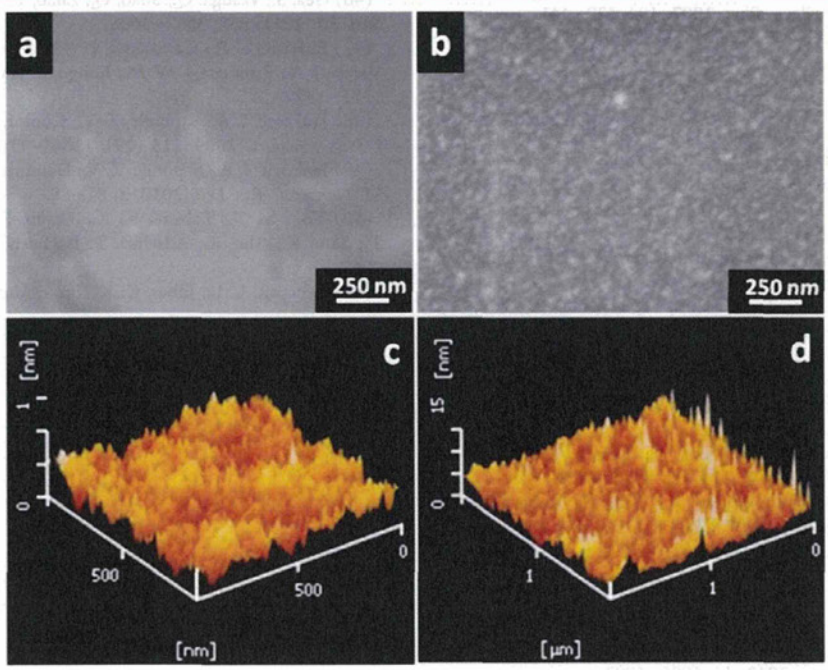

Figure 10. SEM and AFM images of pure polyvinyl alcohol (PVA) film and HfO_2–PVA nanocomposite film (NP load 50 wt %): (a) SEM image of pure film, (b) SEM image of composite film, (c) AFM image of pure film, and (d) AFM image of composite film.

dx.doi.org/10.1021/cg3005739 | Cryst. Growth Des. 2012, 12, 5219–5226

AUTHOR INFORMATION

Corresponding Author

*Tel: (+ 81)-22-217-6321. Fax: (+ 81)-22-217-6321. E-mail: ajiri@tagen.tohoku.ac.jp.

Notes

The authors declare no competing financial interest.

ACKNOWLEDGMENTS

This work was supported by JSPS Grant-in-Aid for Scientific Research (S) 20226015. The authors gratefully acknowledge the Tohoku university international advanced research and education organization (IAREO) for their financial support. The authors also gratefully acknowledge Mr. Takamichi Miyazaki for obtaining the HRTEM results.

REFERENCES

(1) Lee, L. H.; Chen, W. C. *Chem. Mater.* **2001**, *13*, 1137−1142.

(2) Yuwono, A. H.; Liu, B.; Xue, J.; Wang, J.; Elim, H. I.; Ji, W.; Li, Y.; White, T. J. *J. Mater. Chem.* **2004**, *14*, 2978−2987.

(3) Lu, C.; Cui, Z.; Li, Z.; Yang, B.; Shen, J. *J. Mater. Chem.* **2003**, *13*, 526−530.

(4) Lee, S.; Shin, H. J.; Yoon, S. M.; Yi, D. K.; Choi, J. Y.; Paik, U. *J. Mater. Chem.* **2008**, *18*, 1751−1755.

(5) Elim, H.; Cai, B.; Kurata, Y.; Sugihara, O.; Kaino, T.; Adschiri, T.; Chu, A. L.; Kambe, N. *J. Phys. Chem. B* **2009**, *113*, 10143−10148.

(6) Lu, C.; Guan, C.; Liu, Y.; Cheng, Y.; Yang, B. *Chem. Mater.* **2005**, *17*, 2448−2454.

(7) Bae, W. J.; Trikeriotis, M.; Sha, J.; Schwartz, E. L.; Rodriguez, R.; Zimmerman, P.; Giannelis, E. P.; Ober, C. K. *J. Mater. Chem.* **2010**, *20*, 5186−5189.

(8) Zimmerman, P. A.; Rice, B. J.; Piscani, E. C.; Liberman, V. *Proceedings of SPIE: The International Society for Optical Engineering 7274*, art. no. 727420.

(9) Meskin, P. E.; Gavrilov, A. I.; Maksimov, V. D.; Ivanov, V. K.; Churagulov, B. P. *Russ. J. Inorg. Chem.* **2007**, *52*, 1648−1656.

(10) Meskin, P. E.; Sharikovb, F. Y.; Ivanov, V. K.; Churagulov, B. R.; Tretyakov, Y. D. *Mater. Chem. Phys.* **2007**, *104*, 439−441.

(11) Pucci, A.; Clavel, G.; Willinger, M. G.; Zitoun, D.; Pinna, N. *J. Phys. Chem. C* **2009**, *113*, 12048−12058.

(12) Buha, J.; Arčon, D.; Niederberger, M.; Djerdj, I. *Phys. Chem. Chem. Phys.* **2010**, *12*, 15537−15543.

(13) Tang, J.; Fabbri, J.; Robinson, R. D.; Zhu, Y.; Herman, I. P.; Steigerwald, M. L.; Brus, L. E. *Chem. Mater.* **2004**, *16*, 1336−1342.

(14) Tirosh, E.; Markovich, G. *Adv. Mater.* **2007**, *19*, 2608−2612.

(15) Buha, J.; Arcon, D.; Niederberger, M.; Djerdj, I. *Phys. Chem. Chem. Phys.* **2010**, *12*, 15537−15543.

(16) Zhang, J.; Ohara, S.; Umetsu, M.; Naka, T.; Hatakeyama, Y.; Adschiri, T. *Adv. Mater.* **2007**, *19*, 203−206.

(17) Taguchi, M.; Takami, S.; Adschiri, T.; Nakane, T.; Sato, K.; Naka, T. *CrystEngComm* **2011**, *13* (8), 2841−2848.

(18) Togashi, T.; Naka, T.; Asahina, S.; Sato, K.; Takami, S.; Adschiri, T. *Dalton Trans.* **2011**, *40* (5), 1073−1078.

(19) Rangappa, D.; Naka, T.; Ohara, S.; Adschiri, T. *Cryst. Growth Des.* **2010**, *10* (1), 11−15.

(20) Rangappa, D.; Ohara, S.; Naka, T.; Kondo, A.; Ishii, M.; Adschiri, T. *J. Mater. Chem.* **2007**, *17* (41), 4426−4429.

(21) Rangappa, D.; Naka, T.; Kondo, A.; Ishii, M.; Kobayashi, T.; Adschiri, T. *J. Am. Chem. Soc.* **2007**, *129* (36), 11061−11066.

(22) Mousavand, T.; Ohara, S.; Naka, T.; Umetsu, M.; Takami, S.; Adschiri, T. *J. Mater. Res.* **2010**, *25* (2), 219−223.

(23) Sahraneshin, A.; Takami, S.; Minami, K.; Hojo, D.; Arita, T.; Adschiri, T. *Prog. Cryst. Growth Charact. Mater.* **2012**, *58*, 43−50.

(24) Sahraneshin, A.; Takami, S.; Hojo, D.; Arita, T.; Minami, K.; Adschiri, T. *CrystEngComm* **2012**, *14*, 6085−6092.

(25) Pileni, M. P. *Nat. Mater.* **2003**, *2*, 145−150.

(26) Petit, C.; Lixon, P.; Pileni, M. P. *J. Phys. Chem.* **1993**, *97*, 12974−12983.

(27) Park, J.; Joo, J.; Kwon, S. G.; Jang, Y.; Hyeon, T. *Angew. Chem., Int. Ed.* **2007**, *46*, 4630−4660.

(28) Quinlan, F. T.; Kuther, J.; Tremel, W.; Knoll, W.; Risbud, S.; Stroeve, P. *Langmuir* **2000**, *16*, 4049−4051.

(29) Iijima, M.; Kamiya, H. *KONA Powder Part. J.* **2009**, *27*, 119−129.

(30) Rutnakornpituk, M.; Puangsin, N.; Theamdee, P.; Rutnakornpituk, B.; Wichai, U. *Polymer* **2011**, *52* (4), 987−995.

(31) Robinson, I.; Alexander, C.; Tung, L. D.; Fernig, D. G.; Thanh, N. T. K. *J. Magn. Magn. Mater.* **2009**, *321*, 1421−1423.

(32) Sahraneshin, A.; Takami, S.; Hojo, D.; Minami, K.; Arita, T.; Adschiri, T. *J. Supercrit. Fluids* **2012**, *62*, 190−196.

(33) Barraud, E.; Bégin-Colin, S.; Caër, G. L.; Villieras, F.; Barres, O. *J. Solid State Chem.* **2006**, *179*, 1842−1851.

(34) Vasilev, V. P.; Lytkin, A. I.; Chernyavskaya, N. V. *J. Therm. Anal. Calorim.* **1999**, *55*, 1003−1009.

(35) Gong, W.; Fu, Z.; Zhou, S.; Du, S.; Zhang, S.; Dai, Z.; Li, W. *J. Electrochem. Soc.* **2010**, *157* (10), J338−J341.

(36) Jia, C.; Cheng, Y.; Bao, F.; Chen, D.; Wang, Y. *J. Cryst. Growth* **2006**, *294* (2), 353−357.

(37) Ren, Y.; Ma, J.; Wang, Y.; Zhu, X.; Lin, B.; Liu, J.; Jiang, X.; Tao, J. *J. Am. Ceram. Soc.* **2007**, *90* (4), 1251−1254.

(38) Zhang, X.; Sui, C.; Gong, J.; Su, Z.; Qu, L. *J. Phys. Chem. C* **2007**, *111*, 9049−9054.

(39) Stefanic, G.; Musíc, S.; Moĺcanov, K. *J. Alloys Compd.* **2005**, *387*, 300−307.

(40) Kobayashi, T.; Sasaki, T.; Takagi, I.; Moriyama, H. *J. Nucl. Sci. Technol.* **2007**, *44* (1), 90−94.

(41) Denkewicz , R. P., Jr.; TenHuisen, K. S.; Adair, J. H. *J. Mater. Res.* **1990**, *5* (11), 2698−2705.

(42) Stefamc, G.; Popovid, S.; Musid, S. *Thermochim. Acta* **1997**, *303*, 31−39.

(43) Takami, S.; Ohara, S.; Adschiri, T.; Wakayama, Y.; Chikyow, T. *Dalton Trans.* **2008**, 5442−5446.

(44) Qiu, Y.; Xu, G. L.; Yan, K.; Sun, H.; Xiao, J.; Yang, S.; Sun, S. G.; Jind, L.; Deng, H. *J. Mater. Chem.* **2011**, *21*, 6346−6353.

(45) Ge, J.; Hu, Y.; Biasini, M.; Beyermann, W. P.; Yin, Y. *Angew. Chem., Int. Ed.* **2007**, *46*, 4342−4345.

(46) Gea, S.; Wanga, Q.; Shao, Q.; Zhao, Y.; Yang, X.; Wang, X. *Appl. Surf. Sci.* **2011**, *257*, 3657−3665.

(47) Eliziário, S. A.; Cavalcante, L. S.; Sczancoski, J. C.; Pizani, P. S.; Varela, J. A.; Espinosa, J. W. M.; Longo, E. *Nanoscale Res. Lett.* **2009**, *4*, 1371−1379.

(48) Jankovic, I. A.; Saponjic, Z. V.; Comor, M. I.; Nedeljkovic, J. M. *J. Phys. Chem. C* **2009**, *113* (29), 12645−12652.

(49) Jankovic, I. A.; Šaponjic, Z. V.; Džunuzovic, E. S.; Nedeljkovic, J. M. *Nanoscale Res. Lett.* **2010**, *5*, 81−88.

(50) Togashi, T.; Takami, S.; Kawakami, K.; Yamamoto, H.; Naka, T.; Sato, K.; Abe, K.; Adschiri, T. *J. Mater. Chem.* **2012**, *22*, 9041−9045.

(51) Beecroft, L. L.; Ober, C. K. *Chem. Mater.* **1997**, *9*, 1302−1317.

View Online / Journal Homepage / Table of Contents for this issue
Dynamic Article Links

CrystEngComm

Cite this: *CrystEngComm*, 2012, **14**, 6085–6092

www.rsc.org/crystengcomm

PAPER

Mechanistic study on the synthesis of one-dimensional yttrium aluminum garnet nanostructures under supercritical hydrothermal conditions in the presence of organic amines

Ameneh Sahraneshin,[ab] Seiichi Takami,[b] Daisuke Hojo,[c] Toshihiko Arita,[b] Kimitaka Minami[d] and Tadafumi Adschiri*[bcd]

Received 4th April 2012, Accepted 18th June 2012
DOI: 10.1039/c2ce25494h

Novel one-dimensional nanostructures of yttrium aluminum garnet were synthesized under supercritical hydrothermal conditions in the presence of organic amine molecules. In addition, the effect of different reaction parameters such as the presence of organic amine molecules, pH of the precursor solution, and the state of water (sub- or supercritical conditions) on the morphology of the final product was investigated. In this paper, considering the simultaneous effects of these different parameters, a new electrostatic model is proposed to explain the formation mechanism of the obtained nanostructures.

Introduction

Nanomaterials with new structures could display novel properties that could be useful in special applications such as the fabrication of optoelectronic nanodevices. There is a strong correlation between the size, morphology, and structure of nanomaterials and their optical, electrical, catalytic, and other properties.[1–7] In addition, controlling the size, morphology, and structure of nanocrystals is academically and technologically important. This is because the synthesis of nanocrystals with new structures opens up new windows for studying the mechanism of crystal growth. Among the numerous inorganic nanomaterials with distinct structural and geometrical features, one-dimensional (1D) nanomaterials such as nanowires, nanotubes, nanorods, and nanobelts have attracted special attention because of their important role as building blocks for the fabrication of future nanoscale devices. [8–10] In the fabrication of optoelectronic nanodevices, particularly high-performance lasers, the alignment of nanoparticles (NPs) to achieve better control of the flow of light is a critical issue. One-dimensional nanostructures are preferable morphologies for such purposes.[11–18]

Among the various methods for synthesizing shape-controlled nanostructures, the template-directed synthesis method is the most commonly used approach.[19] Moreover, typical available templates include organic templates,[20] porous membrane-based templates,[14] and pre-existing 1D nanostructured templates.[19] The use of organic templates as structure-directing agents has attracted considerable attention because in addition to controlling the shapes of nanostructures, they play a key role in the synthesis of organic–inorganic hybrid nanomaterials.[20–23] However, the synthesis of nanostructures using the organic templates has several drawbacks including polycrystallinity of the products, the relatively limited quantity of structures that can be produced, the necessity of a calcination step for sample purification, and the large amount of organics that is required while using organic templates.[24]

In our previous paper, we reported that the morphology of yttrium aluminum garnet (YAG) NPs can be controlled *via* a facile supercritical hydrothermal method that involves incorporation of organic molecules into the reaction mixture.[25] In this study, we synthesized novel 1D YAG nanostructures with interesting zigzag surfaces using oleylamine as the surfactant. YAG, with the chemical formula $Y_3Al_5O_{12}$, is a transparent material with numerous applications. In addition to its high refractive index, YAG's excellent physical, chemical, and optical properties make it an excellent candidate as a host material in solid state lasers.[26–34]

The simplicity of the experimental procedure with a short reaction time of 10 min, the ability to control the growth direction of nanostructures by addition of a small amount of organics, and the formation of nanostructures with a single crystalline nature are interesting aspects of this work. Because the synthesis of nanocrystals with special structures and a desired size and morphology has significant potential in practical applications, there is a need to understand the mechanism of nanocrystal growth. Therefore, a systematic study of the shape-guiding processes is necessary. Herein, we report the results of a

[a]*Graduate School of Engineering, Tohoku University, 6-6 Aramaki Aza Aoba, Aoba-ku, Sendai, 980-8579, Japan*
[b]*Institute of Multidisciplinary Research for Advanced Materials, Tohoku University, 2-1-1 Katahira, Aoba-ku, Sendai, 980-8577, Japan. E-mail: ajiri@tagen.tohoku.ac.jp; Fax: (+ 81)-22-217-6321; Tel: (+ 81)-22-217-6321*
[c]*World Premier International Research Center-Advanced Institute for Materials Research (WPI-AIMR), Tohoku University, 2-1-1 Katahira, Aoba-ku, Sendai, 980-8577, Japan*
[d]*New Industry Creation Hatchery Center, Tohoku University, 6-6-10 Aramaki Aza Aoba, Aoba-ku, Sendai, 980-8579, Japan*

systematic study on the formation mechanism of novel 1D YAG nanostructures *via* an investigation of the effects of different parameters such as the role of organic capping agents, pH of the precursor solution, and the state of the water (sub- or supercritical conditions).

Materials and methods

Precursor 1

In a typical synthesis procedure, a stoichiometric yttrium aluminum hydroxide solution was first prepared by dissolving 0.130 g aluminum nitrate nonahydrate ([$Al(NO_3)\cdot 3.9H_2O$], 99.99%) and 0.085 g yttrium nitrate hexahydrate ([$Y(NO_3)\cdot 3.6H_2O$], 99.99%) in 3.0 mL deionized water and then adding 7.0 mL of a 0.25 M potassium hydroxide solution (KOH, 99.99%) dropwise with continuous stirring. By addition of a few more drops of the 0.25 M KOH solution, the final pH of this final hydroxide solution was adjusted to 9.95, which is the optimum pH for inhibiting the formation of impurities such as aluminum oxyhydroxide (AlOOH), yttrium oxyhydroxide (YOOH), yttrium aluminum monoclinic (YAM), and yttrium aluminum perovskite (YAP).[34]

Precursor 2

The same quantities of aluminum and yttrium nitrates as used for the preparation of precursor 1 were dissolved in 5.5 mL of deionized water, and then, 4.5 mL of the 0.25 M KOH solution was added dropwise with continuous stirring. The final pH of the hydroxide solution was approximately 5.50.

Precursor 3

The same quantities of aluminum and yttrium nitrates as used for the preparation of precursor 1 were dissolved in 1.5 mL of deionized water, and then, 8.5 mL of the 0.25 M KOH solution was added dropwise with continuous stirring. The final pH of the hydroxide solution was approximately 12.5.

Nanoparticles synthesis

The prepared hydroxide solution (2.5 mL) of aluminum and yttrium nitrates and 7.50×10^{-4} mol alkylamine (*e.g.* oleylamine, decylamine, dodecylamine, or hexadecylamine) were poured into a pressure-resistant tubular reactor with an inner volume of 5.0 mL. The molar ratio of (Y + Al) to amine was 1 : 6. The reactor was sealed and placed in an electrical furnace whose temperature was set at 420 °C in advance. The reaction was continued for 10 min and then was terminated by quenching the reactor in a room temperature water bath. The product, which was a whitish aqueous mixture of synthesized particles, unreacted hydroxides, and unreacted organic molecules, was collected using 3.0 mL of hexane and then was allowed to settle for 1 h in order to separate the organic and aqueous phases. Next, the aqueous phase was removed and the remainder was subjected to three cycles of centrifugation/decantation using ethanol to remove any unreacted organic molecules. Finally, the particles were dispersed in cyclohexane and freeze dried under vacuum for 6 h.

The crystalline structure of the particles was identified using an X-ray diffractometer (XRD, Rigaku Ultima IV) with Cu-Kα radiation in a 2θ–θ setup. The 2θ angle was scanned between 10° and 80°. The crystalline nature of the products was also investigated using a scanning transmission electron microscope (STEM). In addition, the size and morphology of the particles were analyzed using a scanning electron microscope (SEM, Hitachi S-4200) at an accelerating voltage of 15 kV and a transmission electron microscope (TEM, Hitachi H7650) at 100 kV. The elemental analysis was performed using energy-dispersive X-ray spectroscopy (EDX) using a Hitachi S-4500 microscope operating at 15 kV. The collected spectra were analyzed using the Quantex software program.

Results

In this section, we established the characteristics of the products and then, examine the effects resulting from the use of different reaction conditions.

Characteristics of the basic nanostructures

The morphology and size of the products obtained from precursor 1 in the presence of oleylamine were revealed by their TEM and SEM images, as illustrated in Fig. 1a and b. The images show that the products are composed of 1D nanostructures. The magnified TEM image (Fig. 1c) shows that the obtained structures have a novel zigzag surface. Each nanostructure is about 70 nm in diameter and 1 μm in length. The corresponding STEM image (Fig. 1d) and nanobeam diffraction (NBD) pattern taken along the [−210] zone axis (inset of Fig. 1d) reveal that the obtained nanostructures have a single crystalline nature and have preferentially grown along the <001> direction. The X-ray diffraction pattern (XRD) in Fig. 2a confirms the crystallinity of the obtained nanostructures. All reflection peaks in the XRD pattern can be readily indexed to the standard pattern of cubic YAG (JCPDS No. 33-0040).

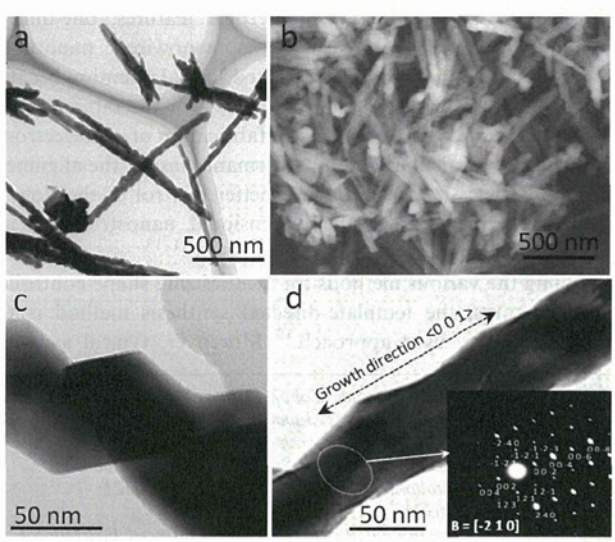

Fig. 1 TEM (a and c), SEM (b), STEM (d), and SAED patterns (inset of d) of as-synthesized particles using precursor 1 (pH = 9.95) in the presence of oleylamine.

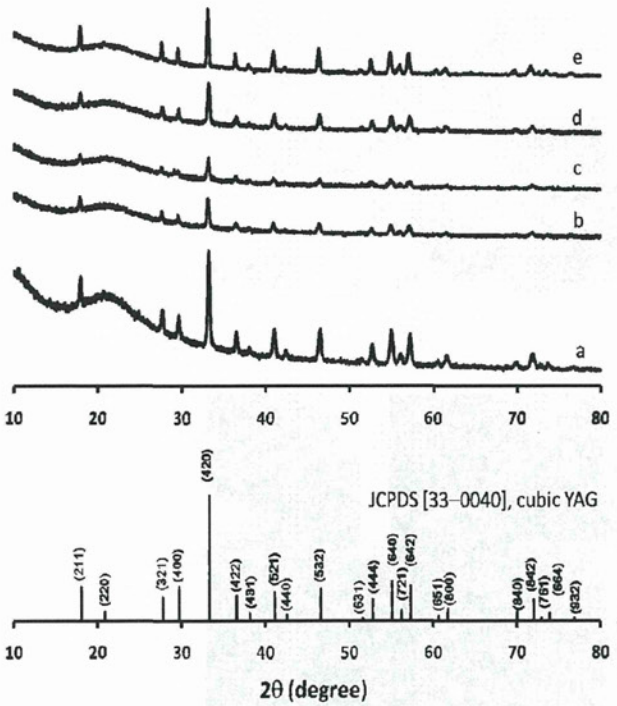

Fig. 2 XRD pattern of as-synthesized particles using precursor 1 modified with a) oleylamine, b) decylamine, c) dodecylamine, d) hexadecylamine, and e) without a modifier.

Effect of the amine

Comparison of the morphology of these nanostructures (Fig. 1) with that of the nanoparticles synthesized without an organic modifier (Fig. 3a) reveals that the presence of oleylamine molecules significantly influences nanoparticle morphology. This is because in the absence of organic molecules, 500 nm cubic nanoparticles were synthesized. To confirm the role of the amine molecules in the formation of the 1D YAG nanostructures, other alkyl amines with different alkyl chain lengths (*e.g.* decylamine, dodecylamine, and hexadecylamine) were used in the synthesis of the nanoparticles. According to the TEM images in Fig. 3b–d, the products exhibited the same 1D morphology with zigzag surfaces in the presence of all amine modifiers. In addition, the XRD patterns of the products (Fig. 2b–d) show that all samples were YAG crystals with a pure cubic phase.

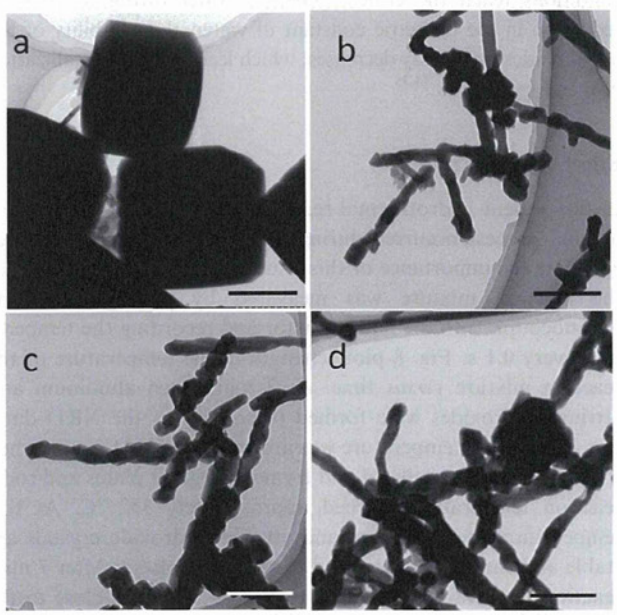

Fig. 3 TEM images of as-synthesized particles using precursor 1 in the a) absence of organic modifiers and presence of b) n-decylamine, c) n-dodecylamine, and d) 1-hexadecylamine. Scale bars show 200 nm.

On the basis of the above-mentioned observations, it can be concluded that the NH_2 group plays an indispensable role in the formation of the 1D YAG nanostructures. It has previously been reported that amines might act as crystal facet inhibitors in the crystal growth process.[23,35–37] This is because amine molecules can cover particular crystal facets of initial crystals and change the surface energy of these facets, causing the formation of anisotropic structures. To investigate this theory, the synthesis was repeated using different amounts of oleylamine. The TEM images of the products are shown in Fig. 4. In the absence of oleylamine molecules, cubic YAG NPs were synthesized (Fig. 4a). Addition of 3.75×10^{-4} mol oleylamine to the reaction mixture affected the shape of the particles and some irregular YAG structures were formed (Fig. 4b). Moreover, increasing the amount of oleylamine to 7.50×10^{-4} mol resulted in the formation of 1D YAG nanostructures (Fig. 4c).

Effect of pH

The function of organic molecules during hydrothermal synthesis might depend on the reaction environment, *i.e.*, the way that organic molecules dissociate and produce active ions that tend to be attracted to the inorganic surfaces. Therefore, the pH of the reaction mixture could play an important role. To confirm the effect of pH on the synthesis of the nanoparticles, the procedure was repeated using precursors with a different starting pH (neglecting the inhibition of the formation of impurities such as yttrium or aluminum oxyhydroxides, YAM, and YAP). Fig. 5 depicts the corresponding TEM images of the samples that were synthesized using precursors 2 (pH 5.5) and 3 (pH 12.5). As can be seen in the TEM images, the use of the low-pH precursor resulted in highly aggregated structures approximately 120 nm in diameter with undeveloped hexagonal boundaries (Fig. 5a), indicating that under such conditions, the amine molecules could not control nanocrystal growth. On the other hand, using the highly alkaline precursor, semispherical nanocrystals were formed (Fig. 5b). This result suggests that under highly basic conditions, nanocrystal growth was controlled in almost all directions. These results reveal the strong effect of pH on the ability of amine molecules to control the morphology of the products.

Shape evolution of the nanoparticles

To determine the formation mechanism of the 1D YAG nanostructures during the supercritical hydrothermal reaction, the shape evolution of the structures during the reaction was investigated. YAG particles were synthesized from precursor 1 in the presence of oleylamine molecules with reactions times of

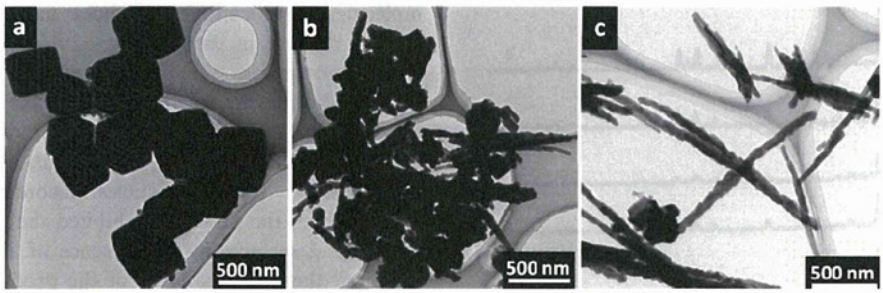

Fig. 4 YAG nanostructures synthesized in the presence of oleylamine: a) 0 mol, b) 3.75×10^{-4} mol and c) 7.5×10^{-4} mol.

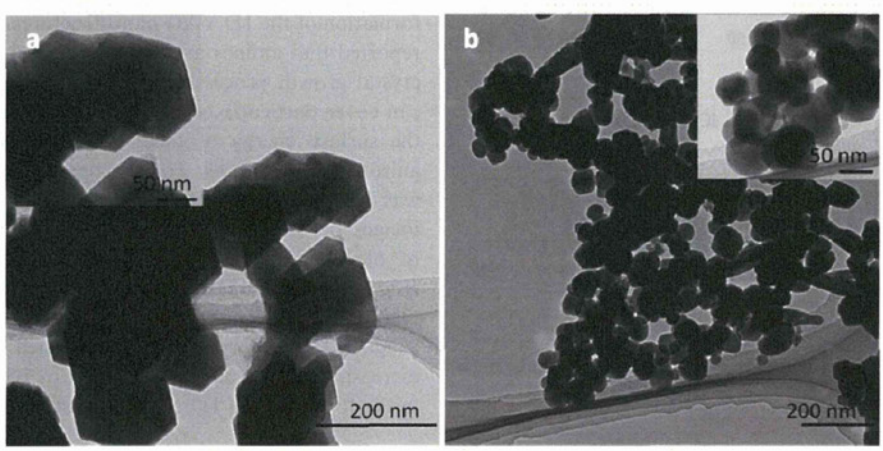

Fig. 5 TEM images of the particles synthesized in the presence of oleylamine using a) precursor 2 (pH = 5.5) and b) precursor 3 (pH = 12.5).

3–10 min. Fig. 6 shows the TEM images of the products obtained after 3, 5, 7, and 8 min. The crystalline phase of the products were identified from their XRD patterns as shown in Fig. 7.

By comparing the positions of the diffraction peaks in the XRD patterns of the products with those in the JCPDS patterns of AlOOH, YOOH, and YAG, it was found that in the early stages of the reaction (after 3 min), aluminum oxyhydroxide and yttrium hydroxide were formed (Fig. 6a and 7a). After 5 min, aluminum and yttrium hydroxides were crystallized and some irregular plates and nanorods were formed (Fig. 6b and 7b). To determine the elemental composition of these phases, elemental analysis was performed using energy-dispersive X-ray spectroscopy (EDX). The obtained EDX patterns of the nanorods and nanoplates are shown in the inset of Fig. 6b. From these EDX patterns, it was determined that the nanorods were composed of yttrium hydroxide, while the nanoplates comprised aluminum oxyhydroxide and a small portion of yttrium hydroxide. After 7 min, the intensity of the XRD peaks decreased, indicating the dissolution of the hydroxides (Fig. 6c and 7c). However, within 8 min, the dissolved hydroxides recrystallized and formed their combined oxide (YAG; Fig. 6d and 7d). The EDX pattern of the final product (inset of Fig. 6d) shows the formation of a composite of aluminum and yttrium oxide.

Crystallization of the metal hydroxides and their dissolution and ultimate recrystallization in the oxide phase is a temperature-dependent process. Such a dissolution–recrystallization process that is a function of reaction temperature has been previously reported by Hakuta and coworkers for the supercritical hydrothermal synthesis of YAG : Tb NPs.[34,38] In general, the solubility of the metal oxides and metal hydroxides in neutral and alkaline aqueous solutions increases with temperature. However, when reaction conditions reach the critical point of water owing to a sharp reduction in the dielectric constant of water, the solubility of the metal oxides drastically decreases, which leads to the crystallization of metal oxide NPs.[34,38]

Effect of temperature

In the present hydrothermal reaction, the dissolution–recrystallization process occurred during the heating stages. To further elucidate the importance of this issue, the temperature profile of the reaction mixture was measured by placing a K-type thermocouple into the batch reactor and recording the temperature every 0.1 s. Fig. 8 plots changes in the temperature of the reaction mixture *versus* time. At 3 min, when aluminum and yttrium hydroxides were formed (according to the XRD data, Fig. 7), reaction temperature was around 302 °C. At 5 min, when the hydroxides crystallized and formed irregular plates and rods, reaction temperature reached approximately 352 °C. At this temperature, the aluminum and yttrium hydroxide crystals are stable and cannot be converted to the oxide phase. After 7 min, reaction temperature increased to 378 °C, which is close to the critical temperature of water (reaction pressure at 378 °C is around 26 MPa). From the XRD pattern, it can be seen that the intensity of the XRD peaks was clearly reduced, indicating the dissolution of the hydroxides under these conditions. When

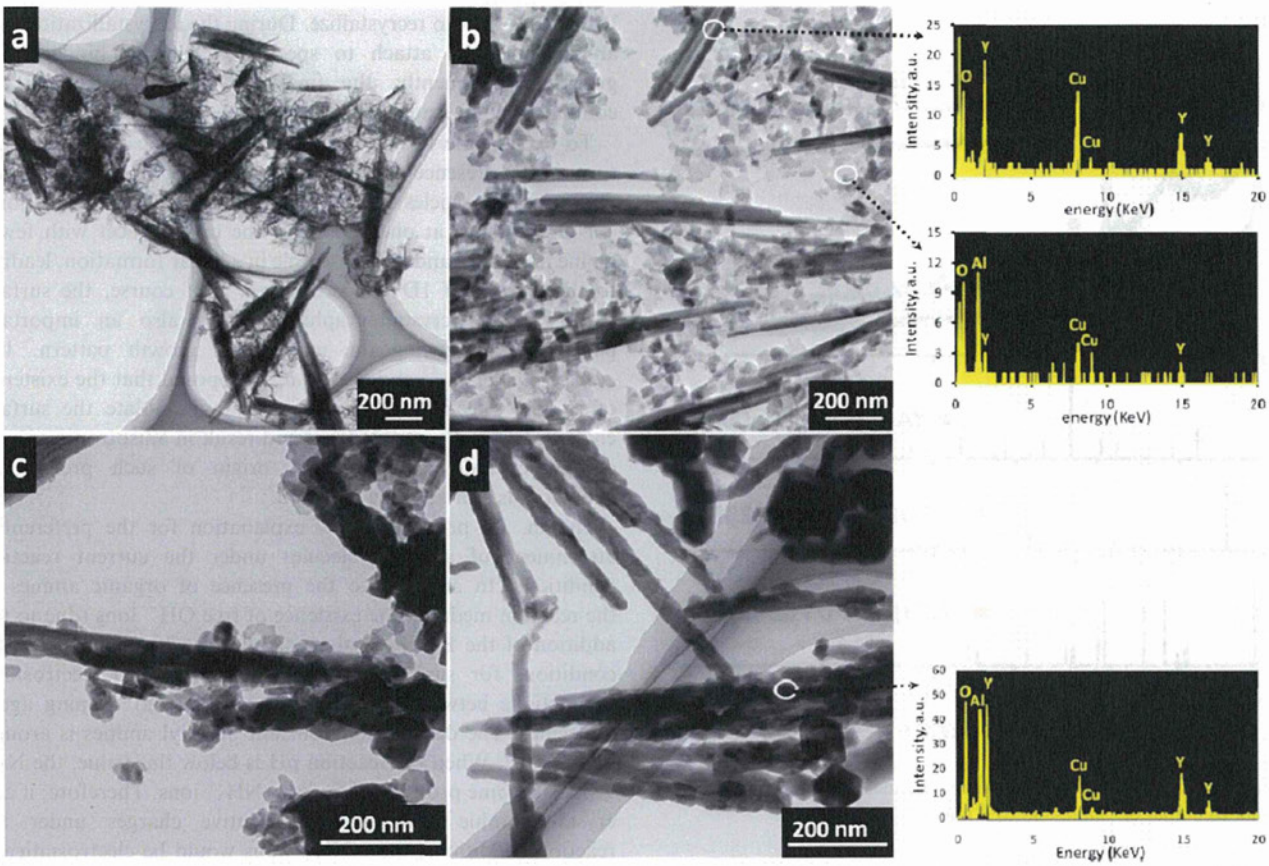

Fig. 6 Shape evolution of the 1D YAG nanostructures after reaction times a) 3 min, b) 5 min, c) 7 min, and d) 8 min. The insets of b) and d) show the EDX patterns of the marked areas in the TEM images.

reaction time reached 8 min, reaction temperature increased to 384 °C (the pressure at 384 °C is 29 MPa). At this point, the reaction medium reached supercritical hydrothermal conditions. After crossing the critical point, the fused aluminum and yttrium hydroxides recrystallized and were converted to the combined oxide (YAG). Hakuta *et al.* and Zheng *et al.* also reported that the water state under supercritical conditions is a critical factor in the crystallization of aluminum and yttrium hydroxides and the formation of YAG particles.[38,29]

Discussion

The formation of a crystal structure involves two fundamental steps: nucleation and growth. Several parameters are responsible for the determination of the final morphology of nanocrystals during these two steps, for example, the crystalline phase of the seed at the nucleating stage, the intrinsic surface energy of different crystallographic surfaces, and the role of surface-selective capping molecules.[39] It is apparent that in the formation of 1D nanostructures, the different growth rates of the crystallographic planes leads to anisotropic crystal growth. There are numerous research reports on the formation of anisotropic nanostructures using the selective absorption behavior of organic capping agents.[23,24,37,40–43] For example, Chen and Sugahara reported the formation of organic–inorganic tungstate-based nanobelts/nanotubes in the presence of n-alkylamines.[36] Zhang *et al.* showed that capping ligands such as oleylamine resulted in a growth rate difference among different surface facets and caused anisotropic crystal growth.[37] In addition, Wang *et al.* conducted a series of experiments to investigate the effect of different organics with absorbing ligands such as alcohols, carboxylic acids, and alkylamines on the formation of anatase titania nanocrystals with different morphologies.[43] They proposed that organic molecules selectively control the growth of nanocrystals to form 1D nanowires or nanorods.

To date, two main possible mechanisms have been proposed to explain the formation of anisotropic nanostructures in the presence of organic molecules. The first hypothesis is that capping agents act as soft templates and through micelle or reverse-micelle orientations, they control the growth of nanostructures in favor of some crystallographic planes.[20,44] In the second hypothesis, the preferential tendency of organic molecules for specific crystal faces has been highlighted as the main reason for anisotropic crystal growth.[23,39,45,46] To achieve a micelle or reverse-micelle orientation of organic molecules, a critical concentration of the surfactant is required.[47] Because we used only a small amount of organics compared to the volume of the reaction environment (nearly a 1 : 8 volume ratio), the second hypothesis, *i.e.*, the preferential attachment of organic molecules to specific crystal faces, seems to be more likely in the present case.

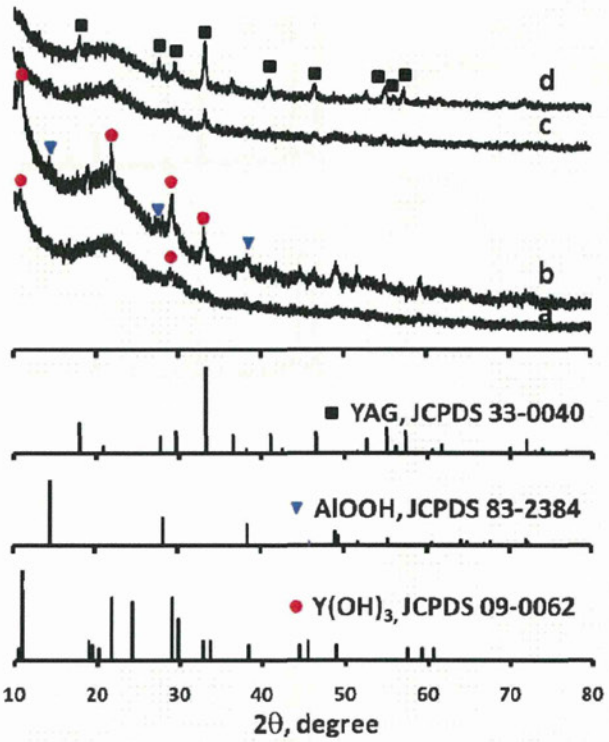

Fig. 7 XRD patterns of the products obtained after reaction times a) 3 min, b) 5 min, c) 7 min, and d) 8 min.

Based on the analysis of morphological changes and the development of the 1D YAG nanostructures, the formation of anisotropic YAG nanostructures in the presence of amine modifiers can be expressed as shown in Scheme 1. First, yttrium and aluminum hydroxides crystallize to form rod- and irregular plate-like structures. When the critical point of water is reached during the heat-up procedure, the hydroxides start to dissolve and diffuse together. After the critical point is crossed, the fused hydroxides start to recrystallize. During the recrystallization, the amine molecules attach to specific facets and hinder their growth; consequently, the final 1D nanostructures of the combined metal oxide (YAG) are formed.

To explain the formation of the metal oxide 1D nanostructures in the presence of amine molecules, Zhong *et al.* proposed that primary particles covered with amine molecules form a joint (M–O–M bond) at one end or at the crystal facet with fewer amine molecules and then assemble in a linear formation, leading to the growth of 1D nanostructures.[23] Of course, the surface energy of the crystallographic faces is also an important parameter influencing the nanocrystal growth pattern. Jun *et al.*,[39] Lee *et al.*,[45] and Seo *et al.*[46] proposed that the existence of surface selective capping agents can modulate the surface energy of crystallographic faces and result in anisotropic growth of nanocrystals. However, the origin of such preferential behaviors is still an open question.

Herein, we propose a new explanation for the preferential attachment of amine molecules under the current reaction conditions. In addition to the presence of organic amines in the reaction medium, the existence of free OH^- ions (due to the addition of the KOH solution) should also be considered. The conditions for surface capping may depend on electrostatic interactions between the inorganic surface and capping agent molecules. The dissociation constant of alkyl amines is around $pK_b = 10.7$. When the reaction pH is below this value, the NH_2 groups become protonated to form NH_3^+ ions. Therefore, if any crystallographic plane carries negative charges under the reaction conditions, these NH_3^+ ions would be electrostatically attracted to that plane and thus control its growth. The preferential tendency of NH_2 groups to attach to the nanocrystal surface probably occurs owing to the variation of the surface properties of the crystal facets under different pH conditions.

The possibility of anisotropic behavior due to the surface acidities of crystal systems that are manifested by the difference in the isoelectric points of different crystallographic planes has been reported previously.[48,49] Kershner and coworker showed

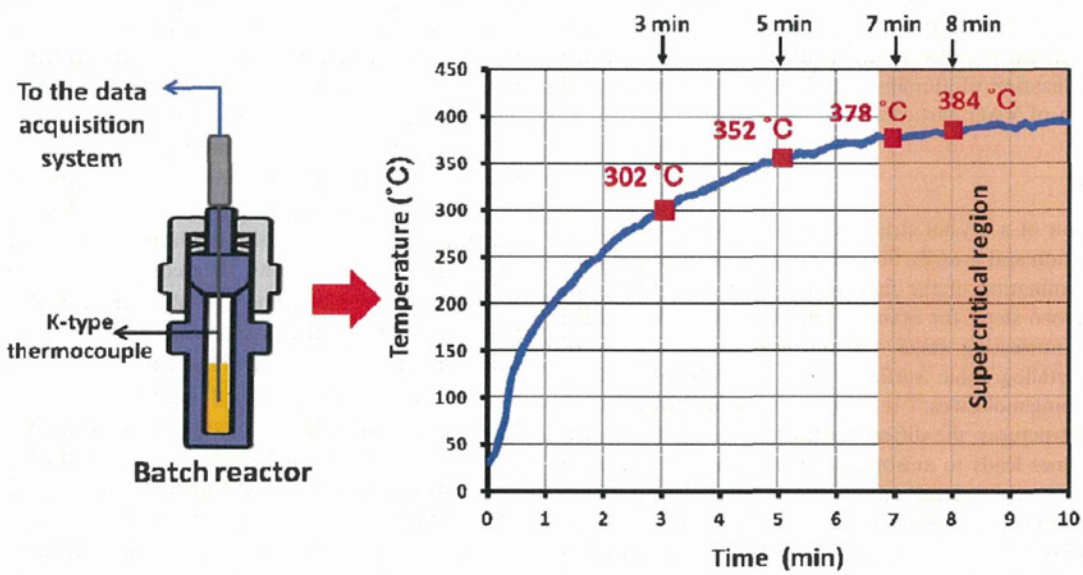

Fig. 8 Temperature profile of the reaction mixture *versus* time. TEM and XRD images were measured at the reaction times shown above the figure.